Journal of Power Sources 182 (2008) 197–222

Contents lists available at ScienceDirect

Journal of Power Sources

journal homepage: www.elsevier.com/locate/jpowsour

A general model of proton exchange membrane fuel cell

Anh Dinh Le, Biao Zhou*

Department of Mechanical, Automotive & Materials Engineering, University of Windsor, Ont., Canada N9B 3P4

ARTICLE INFO

Article history:
Received 18 January 2008
Received in revised form 20 March 2008
Accepted 20 March 2008
Available online 27 March 2008

Keywords:
PEM fuel cell
UDF
FLUENT®
3D
Multi-phase
VOF

ABSTRACT

In this study, a general model of proton exchange membrane fuel cell (PEMFC) was constructed, implemented and employed to simulate the fluid flow, heat transfer, species transport, electrochemical reaction, and current density distribution, especially focusing on liquid water effects on PEMFC performance. The model is a three-dimensional and unsteady one with detailed thermo-electrochemistry, multi-species, and two-phase interaction with explicit gas–liquid interface tracking by using the volume-of-fluid (VOF) method. The general model was implemented into the commercial computational fluid dynamics (CFD) software package FLUENT® v6.2, with its user-defined functions (UDFs). A complete PEMFC was considered, including membrane, gas diffusion layers (GDLs), catalyst layers, gas flow channels, and current collectors. The effects of liquid water on PEMFC with serpentine channels were investigated. The results showed that this general model of PEMFC can be a very useful tool for the optimization of practical engineering designs of PEMFC.

© 2008 Elsevier B.V. All rights reserved.

1. Introduction

In recent years, high-performance computing and advanced numerical algorithms have allowed researchers to model proton exchange membrane fuel cell (PEMFC) systems as well as individual components with greater fidelity than ever before. In general, PEMFC operations involve simultaneously multi-component, multi-phase, multi-dimensional fluid flow with heat and mass transfer and electrochemical reactions. Hence, a complete mathematical model is necessary to characterize more fully the physical behavior, to aid our understanding of complex phenomena occurring in a fuel cell system and to provide powerful tools for fuel cell design and optimization.

Fuel cell performance is evaluated by the relation between the cell voltage and current density. The voltage loss is mainly caused by the activation loss due to electrochemical reactions, the Ohmic loss due to resistance and fuel crossover and the mass transport loss due to limitation of gas transport inside the cell. During fuel cell operation, by-product water is generated in the cathode catalyst layer in the form of liquid, leading to a gas–liquid flow in the porous media and the channels. On the other hand, due to the low operating temperature of PEMFCs (30–100 °C), excessive humidification could result in water vapor condensation. These could subsequently block the gas flow channels resulting in a lower airflow rate on the cathode side, increasing the voltage loss due to mass transport, thus decreasing fuel cell performance. However, due to the special chemical structure of the proton exchange membrane (PEM), the membrane must be well hydrated to ensure that a sufficient amount of hydrogen ions could cross. Water content is also an important factor that affects the Ohmic resistance in the membrane. Therefore, keeping an appropriate amount of water content in the fuel cell to avoid both membrane dehydration and water vapor condensation has been a critical issue in improving fuel cell performance. In reality, however, it is almost impossible to manage water on both the anode and cathode sides without dehydration and condensation; this is simply because water vapor condensation in the gas flow channels of practical fuel cell applications is unavoidable. Therefore, water management, especially liquid water management, to which many engineers and scientists have recently paid particular attention, has been a critical challenge for a high-performance fuel cell design and optimization.

In the last decade, water management-related studies were performed numerically and experimentally for different purposes and in several ways. Recently, three-dimensional models based on the computational fluid dynamics (CFD) approach have been presented by different commercial CFD software packages such as FLUENT®, CFX®, Star-CD®, and CFDRC®. A CFD modeling of PEMFCs which simultaneously considered the electrochemical kinetics, current distributions, hydrodynamics, and multi-component transport was conducted by Um et al. [1]. A three-dimensional numerical simulation of a straight gas flow channel in a PEMFC was performed by Dutta et al. [2] using a commercial CFD software FLUENT®. Hontanon et al. [3] also employed FLUENT® to implement their 3D, stationary gas flow model. A study exploring the steady-state gas

* Corresponding author. Tel.: +1 519 253 3000x2630; fax: +1 519 973 7007.
E-mail address: bzhou@uwindsor.ca (B. Zhou).

0378-7753/$ – see front matter © 2008 Elsevier B.V. All rights reserved.
doi:10.1016/j.jpowsour.2008.03.047

Nomenclature

a	water activity
A_s	heat transfer surface area, m^2
A_{surf}	reactive surface area, m^2
c_f	concentration of sulfonic acid ions (HSO_3^-), $kmol\,m^{-3}$
c_p	specific heat capacity, $J\,kg^{-1}\,K^{-1}$
C_i	species concentration i, $kmol\,m^{-3}$
D_i	diffusion coefficient of species i in gas mixture, $m^2\,s^{-1}$
F	Faraday constant, $9.6487 \times 10^7\,C\,kmol^{-1}$
h	convective heat transfer, $W\,m^{-2}\,K^{-1}$
h_{H_2O}	the enthalpy of formation of water vapor, $N\,m\,kg^{-1}$
I	current density, $A\,m^{-2}$
I_{ave}	average current density, $A\,m^{-2}$
J	mass flux, $kg\,m^{-2}\,s^{-1}$
k_{eff}	effective thermal conductivity, $W\,m^{-1}\,K^{-1}$
M_i	molecular weight of species i in gas mixture, $kg\,kmol^{-1}$
n_d	electro-osmotic drag coefficient
n_f	charge number of the sulfonic acid ion
P	pressure, Pa
P_i	partial pressure of species i, Pa
R	universal gas constant, $8314\,J\,kmol^{-1}\,K^{-1}$
$\dot{Q}$	heat rate, W
R_{cat}, R_{an}	volumetric current density, $A\,m^{-3}$
S	source term
t	time, s
T	temperature, K
u, v, w	velocities in X, Y, and Z directions, respectively, $m\,s^{-1}$
V_{oc}	open-circuit potential, V
V_{cell}	cell potential, V
V_{ref}	reference potential, V
$\mathcal{V}$	volume, m^3
X_i	mole fraction of species i
Y_i	mass fraction of species i

Greek symbols

α	transfer coefficient
β	the factor accounts for energy release
γ	concentration dependence
γ_p, γ_T	exponent factors
ε	porosity
θ_w	contact angle, °
η	overpotential, V
κ	surface curvature
κ_p	hydraulic permeability, m^2
κ_ϕ	electrokinetic permeability, m^2
λ	water content
μ	dynamic viscosity, $kg\,m^{-2}\,s^{-1}$
ρ	density of gas mixture, $kg\,m^{-3}$
ρ_i	density of species i, $kg\,m^{-3}$
σ	phase conductivity, $\Omega^{-1}\,m^{-1}$
τ	gaseous permeability, m^2
υ	reaction rate, $kmol\,m^2\,s^{-1}$
ϕ	phase potential, V
φ	relative water content
χ	surface tension coefficient, $N\,m^{-1}$
ω	excess coefficient

Subscripts and superscripts

an	anode
cat	cathode
e	electrochemical reaction
eff	effective
g	gas phase
H_2	hydrogen
H_2O	water
i	species i
in	inlet
l	liquid phase
m	membrane phase
out	outlet
N_2	nitrogen
O_2	oxygen
ref	reference
s	solid phase
sat	saturated
surf	surface
w	water vapor

transport phenomena in micro-scale parallel flow channels was conducted by Cha et al. [4] in which oxygen concentration along a single gas flow channel and other flow patterns that may affect fuel cell performance were discussed. Similarly, gas concentration of a steady-state flow along fuel cell flow channels was obtained numerically by Kulikovsky [5]. However, in all the studies mentioned above, the effects of liquid water were neglected. Yi et al. [6] pointed out that water vapor condensation was inevitable on both the anode and cathode sides of a PEMFC, and they discussed a liquid water removal technique that used a water transport plate to lead excess liquid water to the coolant flow channels by a pressure difference. Wang et al. [7] conducted a two-phase model on PEMFC cathode to address the liquid water saturation. You and Liu [8] also considered liquid water saturation in a straight channel on the cathode side. Both the Refs. [7,8] showed the importance for considering liquid water in numerical modeling of PEMFCs. A 3D model by Natarajan and Nguyen [9] introduced the effects of flow rate, inlet humidity and temperature on the liquid water flooding in the PEMFC cathode. The numerical results of this model were validated with experimental data. Berning and Djilali [10] presented a multi-phase, multi-component 3D model with heat and mass transfer, where liquid water transport in GDLs was numerically modeled by using viscous and capillary effects. This method was also used in a 3D model by Mazumder and Cole [11]. Other approach to deal with two-phase flow in GDLs based on thermodynamic equilibrium conditions was given by Vynnycky and Vynnycky [12]. In this approach, the location of interface between one phase and the other phase was pointed out from its numerical results. In recent years, more two-phase models have been published [13–15], these simulations predicted water flooding inside PEMFCs, and the liquid water effects on PEMFC performances. Large-scale simulations for complex flow field were also performed with experimental validations [15–18].

All the above research papers have significantly contributed to PEMFC research and development. However, by far, to the authors' knowledge, most of the two-phase numerical models have not considered the interface tracking between liquid water and gas. The detailed behaviors of liquid water transport inside the PEMFCs were rarely discussed except for the present authors' previous study [19], which only dealt with part of serpentine channels—the single U-shaped channel. Recently, Zhou et al. [20–22] also conducted two more studies that dealt with liquid water in serpentine and straight parallel fuel cell stacks. The results showed that different designs of gas diffusion layers (GDLs) and flow channels will affect the liquid

water flow patterns significantly, thus influencing the performance of PEMFCs. Djilali and co-workers [23] presented a 2D, numerical investigation of the dynamic behavior of liquid water entering a PEMFC channel through a small hole that was assumed as a GDL pore. In these studies, the water behaviors can give very useful insights about water management only in the cathode channels although the electrochemical reactions were not considered.

Numerical models that considered liquid water in the porous mediums such as GDL were developed in several ways. Nam and Kaviany [24] developed a two-dimensional, two-phase numerical model by considering random carbon fiber mats as the GDL. Single- and two-layer diffusion mediums were both considered to investigate the effective diffusivity and water saturation. Two main factors influencing on two-phase transport in GDL of a PEMFC such as permeability and capillary pressure were also determined via a capillary network model developed by Djilali and co-workers [25]. In addition, the GDL considered as a network of pore bodies and pore throats used to address the liquid water behavior in PEMFC were presented by Fowler and co-workers [26] or Sinha and Wang [27]. A study on the interaction between the GDL and the flow field was performed by Dohle et al. [28] numerically and experimentally. Other models that considered the porous mediums also mainly focused on the porosity of the carbon fiber paper that could influence the performances of PEMFCs [29,30]. However, the detailed flow patterns that liquid water exhibits across the porous medium of GDL was rarely discussed. Based on their previous efforts on water behaviors inside cathode channels, the present author's group further investigated water behaviors inside innovative GDLs [31,32].

Based on the above literature reviews, it is evident that there is an urgent need to develop a general mathematical model with all detailed physics included, e.g., multi-phase with VOF interface-tracking between gas-phase and liquid–water-phase, multi-components, heat and mass transfer, electrochemical reactions, and water-phase-change effects. In this paper, a general model is presented with all parts of PEMFC including membrane, catalyst layers, GDLs, gas flow channels and current collectors.

2. Mathematical model

Fig. 1 schematically shows a disassembling diagram of a PEMFC comprising of two distinct current collectors with flow channels formed on them at both the cathode and anode; an MEA consists of a proton exchange membrane sandwiched between two catalyst layers. Between the current collectors and the MEA, there are two GDLs on both sides. For the sake of simplicity and popularity, the flow channels are in serpentine form. In this paper, the mathematical model considers all the parts shown in Fig. 1a, the computation domain is shown in Fig. 1b, with geometrical parameters listed in Table 1. The computation domain consists of current collectors, flow channels, GDLs, catalyst layers and membrane. The channels are serpentine, total path length for a channel of 115 mm with 1 mm (width) × 1 mm (height) in the cross-section flow area. The species considered are hydrogen, oxygen, water vapor and nitrogen.

2.1. Model assumptions

The assumptions used in developing the model are as follows:

1. Ideal gas law was employed for gaseous species.
2. The fluid flow in the fuel cell was laminar due to the low flow velocities and the small size of gas flow channels.
3. The porous media including membrane, catalyst layers and GDLs were considered to be isotropic.

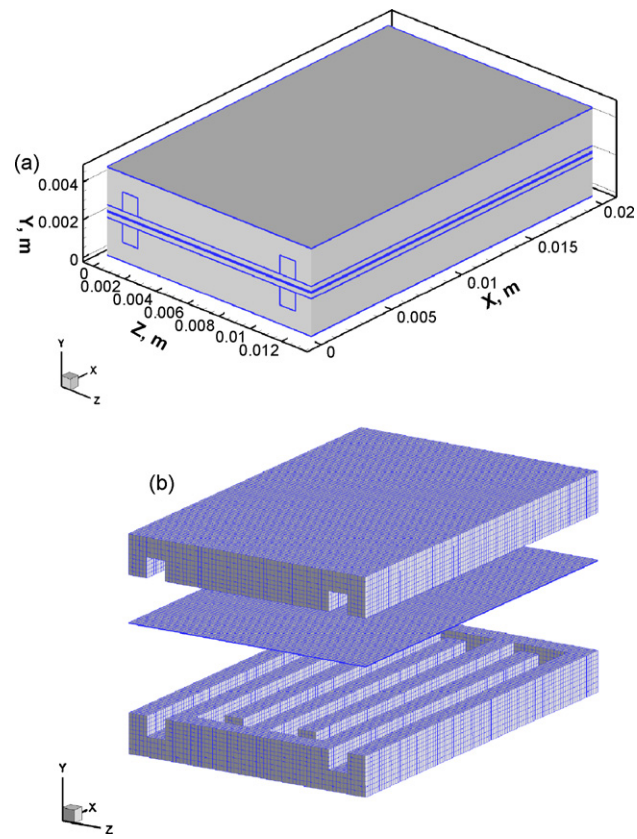

Fig. 1. (a) Schematic diagram of PEMFC and (b) computation domain.

Table 1
Physical properties and parameters

Physical properties or parameters	Value
Total channel length	0.115 m
Channel width	0.001 m
Channel height	0.001 m
Membrane thickness	50×10^{-6} m
GDL thickness	300×10^{-6} m
Catalyst layer thickness	10×10^{-6} m
Anode inlet pressure, $P_{an,in}$	2 atm
Cathode inlet pressure, $P_{cat,in}$	2 atm
Anode and cathode inlet temperature	300 K
Anode inlet excess coefficient, ω_a	3
Cathode inlet excess coefficient, ω_c	3
Relative humidity of anode inlet	20%
Relative humidity of cathode inlet	100%
Open-circuit voltage, V_{oc}	1.15 V
Faraday constant, F	96,487,000 C kmol^{-1}
Gas constant, R	8314 J kmol^{-1} K^{-1}
Anode volumetric reference exchange current density/reference hydrogen concentration, $R_{an}^{ref}/(C_{H_2}^{ref})^{\gamma_{an}}$	7×10^{10} A kmol^{-1}
Cathode volumetric reference exchange current density/reference oxygen concentration, $R_{cat}^{ref}/(C_{O_2}^{ref})^{\gamma_{cat}}$	7×10^{5} A kmol^{-1}
Anode transfer coefficient, α_{an}	0.5
Cathode transfer coefficient, α_{cat}	0.5
Anode concentration dependence, γ_{an}	0.5
Cathode concentration dependence, γ_{cat}	1.0
Factor accounts for energy release, β	0.5
Membrane porosity, ε_{mem}	0.5
Diffusion layer porosity, ε_{GDL}	0.5
Catalyst layer porosity, $\varepsilon_{catalyst}$	0.5
Permeability of porous media, τ	1.76×10^{-11} m^2
Contact angle, θ_w	90°
Surface tension, χ	0.065 N m^{-1}

4. The fuel cell cooling was controlled by forced convection heat transfer.

2.2. Governing equations

2.2.1. Mass conservation equation

The continuity equation is expressed as follows:

$$\frac{\partial \varepsilon\rho}{\partial t} + \nabla\cdot(\varepsilon\rho\vec{v}) = S_{\mathrm{m}} \tag{1}$$

For multi-phase flow, the mixture density is defined as follows [33,34]:

$$\rho = s_{\mathrm{l}}\rho_{\mathrm{l}} + (1-s_{\mathrm{l}})\rho_{\mathrm{g}} \tag{2}$$

$$s_{\mathrm{l}} + s_{\mathrm{g}} = 1 \tag{3}$$

2.2.2. Momentum conservation equation

The momentum equation is dependent on the volume fractions of all phases:

$$\frac{\partial}{\partial t}(\varepsilon\rho\vec{v}) + \nabla(\varepsilon\rho\vec{v}\vec{v}) = -\varepsilon\nabla p + \nabla[\varepsilon\mu\nabla\vec{v}] + S_{\mathrm{v}} \tag{4}$$

$$\text{where } \mu = s_{\mathrm{l}}\mu_{\mathrm{l}} + (1-s_{\mathrm{l}})\mu_{\mathrm{g}} \tag{5}$$

For a mixture of liquid and gas phases, the local mass average velocity v is defined as [33,34]:

$$v = \frac{s_{\mathrm{l}}\rho_{\mathrm{l}}v_{\mathrm{l}} + s_{\mathrm{g}}\rho_{\mathrm{g}}v_{\mathrm{g}}}{s_{\mathrm{l}}\rho_{\mathrm{l}} + s_{\mathrm{g}}\rho_{\mathrm{g}}} \tag{6}$$

The source term for the momentum equation used in the model describes the flow of the fluid through a porous media by using Darcy's drag force. The gravity and surface tension forces were also considered in the momentum equation source term. The source terms for different regions of the fuel cell are given in Table 2.

2.2.3. Volume fraction equation

The tracking of the interface between the phases was accomplished by the solution of a continuity equation for the volume fraction of one (or more) of the phases. The motion of the interface between two immiscible liquids (namely, gas mixture and liquid water) of different density and viscosity in the VOF method was defined by volume fraction of liquid water s_{l} and volume fraction of gaseous phase s_{g} [33].

For volume fraction of liquid water:

$$\frac{\partial}{\partial t}(\varepsilon s_{\mathrm{l}}\rho_{\mathrm{l}}) + \nabla(s_{\mathrm{l}}\rho_{\mathrm{l}}\vec{v}_{\mathrm{l}}) = S_{\mathrm{s}} \tag{7}$$

2.2.4. Energy conservation equation

In this model, the energy balance in terms of temperature change was also considered. In the multi-phase model, the energy equation is also shared among the phases [33,35]:

$$(\rho c_p)_{\mathrm{eff}}\frac{\partial T}{\partial t} + (\rho c_p)_{\mathrm{eff}}(\vec{v}\nabla T) = \nabla(k_{\mathrm{eff}}\nabla T) + S_T \tag{8}$$

where T is the temperature (K) that is defined as

$$T = \frac{s_{\mathrm{l}}\rho_{\mathrm{l}}T_{\mathrm{l}} + (1-s_{\mathrm{l}})\rho_{\mathrm{g}}T_{\mathrm{g}}}{s_{\mathrm{l}}\rho_{\mathrm{l}} + (1-s_{\mathrm{l}})\rho_{\mathrm{g}}} \tag{9}$$

To specify these parameters in porous media, the effective properties were determined:

$$(\rho c_p)_{\mathrm{eff}} = \varepsilon\rho_f c_{p,f} + (1-\varepsilon)\rho_{\mathrm{s}}c_{p,\mathrm{s}} \tag{10}$$

$$k_{\mathrm{eff}} = \varepsilon k_{\mathrm{s}} + (1-\varepsilon)k_f \tag{11}$$

The source term of energy equation for two-phase model may consist of heat from electrochemical reactions, heat of formation of water, Ohmic heating caused by the Ohmic resistance of solid phases and the heat due to phase change. For different zones, the source terms are expressed as in Table 2.

Table 2
The source terms of governing equations

Governing equation	Volumetric source terms and location of application
Conservation of mass	For all parts: $S_{\mathrm{m}} = 0$
Volume fraction	For all parts: $S_{\mathrm{s}} = r_{\mathrm{w}}$, $r_{\mathrm{w}} = c_{\mathrm{r}}\max\left[(1-s_{\mathrm{l}})\frac{P_{\mathrm{wv}}-P_{\mathrm{sat}}}{RT}M_{\mathrm{H_2O}}, -s_{\mathrm{l}}\rho_{\mathrm{l}}\right]$
Conservation of momentum	For gas channels: $S_{\mathrm{v}} = 0$
	For GDLs and void of catalyst layers: $S_{\mathrm{v}} = \rho\vec{g} - \frac{\mu}{\tau}\varepsilon^2\vec{v} + \chi\kappa\frac{2\rho\nabla s_{\mathrm{l}}}{(\rho_{\mathrm{l}}+\rho_{\mathrm{g}})}$
	For membrane: $S_{\mathrm{v}} = \rho\vec{g} - \frac{\mu}{\tau}\varepsilon^2\vec{v} + \chi\kappa\frac{2\rho\nabla s_{\mathrm{l}}}{(\rho_{\mathrm{l}}+\rho_{\mathrm{g}})} + \frac{\kappa_\phi}{\kappa_p}c_f n_f F\nabla\phi_{\mathrm{m}}$
Conservation of energy	For current collectors: $S_T = \frac{I^2}{\sigma_{\mathrm{s}}}$
	For gas flow channel: $S_T = 0$
	For GDL: $S_T = \frac{I^2}{\sigma_{\mathrm{s}}^{\mathrm{eff}}} + r_{\mathrm{w}}h_{\mathrm{L}}$
	For membrane: $S_T = \frac{I^2}{\sigma_{\mathrm{m}}^{\mathrm{eff}}}$
	For catalyst layer: $S_T = \eta R_{\mathrm{an,cat}} + I^2\left(\frac{1}{\sigma_{\mathrm{s}}^{\mathrm{eff}}} + \frac{1}{\sigma_{\mathrm{m}}^{\mathrm{eff}}}\right) + r_{\mathrm{w}}h_{\mathrm{L}}$
Hydrogen transport	For anode catalyst layer: $S_{\mathrm{H_2}} = -\frac{M_{\mathrm{H_2}}}{2F}R_{\mathrm{an}}$
Oxygen transport	For cathode catalyst layer: $S_{\mathrm{O_2}} = -\frac{M_{\mathrm{O_2}}}{4F}R_{\mathrm{cat}}$
Water vapor transport	For anode catalyst layer: $S_{\mathrm{H_2O}} = -\left(\frac{n_{\mathrm{d}}M_{\mathrm{H_2O}}}{F}\right)R_{\mathrm{an}} - r_{\mathrm{w}}$
	For cathode catalyst layer: $S_{\mathrm{H_2O}} = \frac{M_{\mathrm{H_2O}}}{2F}R_{\mathrm{cat}} + \left(\frac{n_{\mathrm{d}}M_{\mathrm{H_2O}}}{F}\right)R_{\mathrm{cat}} - r_{\mathrm{w}}$
Conservation of Charge	For anode catalyst layer: $S_{\mathrm{es}} = -R_{\mathrm{an}}$; $S_{\mathrm{em}} = R_{\mathrm{an}}$
	For cathode catalyst layer: $S_{\mathrm{es}} = R_{\mathrm{cat}}$; $S_{\mathrm{em}} = -R_{\mathrm{cat}}$
	For other parts: $S_{\mathrm{es}} = 0$; $S_{\mathrm{em}} = 0$

2.2.5. Species transport equations

The model predicts the local mass fraction of each species, Y_i, through the solution of a convection–diffusion equation for the ith species. The species transport equations are generally in the following form:

$$\frac{\partial}{\partial t}(\varepsilon\rho Y_i) + \nabla\cdot(\varepsilon\rho\vec{v}Y_i) = D_{i,\mathrm{m}}\nabla^2(\rho Y_i) + S_i \tag{12}$$

where $D_{i,\mathrm{m}}$ is the diffusion coefficient for species i in the mixture [34].

$$D_{i,\mathrm{m}} = \varepsilon^{1.5}(1-s_{\mathrm{l}})^{r_{\mathrm{s}}}D_{i,\mathrm{m}}^0\left(\frac{P_0}{P}\right)^{\gamma_p}\left(\frac{T}{T_0}\right)^{\gamma_T} \tag{13}$$

where $D_{i,\mathrm{m}}^0$ is the diffusion coefficient for species i in the mixture at reference temperature and pressure. The source term in the transport equation is shown in Table 2.

During the operation, the H^+ move from the anode to the cathode and also pull water molecules with them, this is known as the electro-osmotic drag effect. Physically, the water transport rate through the membrane from anode to cathode by electro-osmotic

drag is computed as

$$\dot{m}_{H_2O} = \frac{n_d M_{H_2O}}{F} R_{cat} \tag{14}$$

where n_d is the drag coefficient and is proposed by Springer et al. [36] for Nafion membrane:

$$n_d = \frac{2.5}{22}\lambda \tag{15}$$

where λ is the water content inside the polymer membrane [36].

2.2.6. Conservation of charge

The current transport of electrons through the solid phase and ions through the membrane phase was represented by the following equations [33,35]:

$$\nabla \cdot (\sigma_s \nabla \phi_s) = S_{es} \tag{16}$$

$$\nabla \cdot (\sigma_m \nabla \phi_m) = S_{em} \tag{17}$$

The volumetric source terms S_{es} and S_{em} are defined as volumetric transfer currents. The source term in the equation of charge is shown in Table 2.

The source terms representing transfer current were calculated by using Butler–Volmer equation [33]:

$$R_{an} = R_{an}^{ref}\left(\frac{C_{H_2}}{C_{H_2}^{ref}}\right)^{\gamma_{an}}\left[\exp\left(\frac{\alpha_{an}F\eta_{an}}{RT}\right) - \exp\left(-\frac{\alpha_{cat}F\eta_{cat}}{RT}\right)\right] \tag{18}$$

$$R_{cat} = R_{cat}^{ref}\left(\frac{C_{O_2}}{C_{O_2}^{ref}}\right)^{\gamma_{cat}}\left[\exp\left(-\frac{\alpha_{cat}F\eta_{cat}}{RT}\right) - \exp\left(\frac{\alpha_{an}F\eta_{an}}{RT}\right)\right] \tag{19}$$

The relation between species concentration and species mass fraction is

$$C_i = \frac{Y_i \rho}{M_i} \tag{20}$$

The volumetric transfer current R is driven by the activation overpotential η, which is the potential difference between solid and membrane phases [33,35]:

$$\eta = \phi_s - \phi_m - V_{ref} \tag{21}$$

The reference potential of the electrode V_{ref} is 0 on the anode side and is equal to the open circuit voltage on the cathode side:

$$V_{ref} = 0, \quad \text{on anode side}; \qquad V_{ref} = V_{oc}, \quad \text{on cathode side} \tag{22}$$

The cell potential is then the difference between the cathode and anode solid phase at the terminal collectors (two ends of the cell collectors which are connected to the external electric circuit from the both electrodes).

$$V_{cell} = \phi_{s,cat} - \phi_{s,an} \tag{23}$$

In order to satisfy the conservation of charge, the total current of either electrons or protons coming out from the anode catalyst layer must be equal to the total current coming into the cathode catalyst layer and must be equal to the total current caused by the proton movement through the membrane [35]:

$$\int_{V_{an}} R_{an} d\cancel{V} = \int_{V_{cat}} R_{cat} d\cancel{V} \tag{24}$$

The average current density is the total current generated in the fuel cell divided by the geometric area:

$$I_{ave} = \frac{1}{A}\int_{V_{an}} R_{an} d\cancel{V} = \frac{1}{A}\int_{V_{cat}} R_{cat} d\cancel{V} \tag{25}$$

2.3. Water transport and its effect on the properties of porous media

Water is formed in the cathode catalyst layer by electrochemical reactions—an amount of oxygen is consumed and an amount of water is produced. Due to the proton movement from the anode to the cathode through the membrane, water molecules are pulled with the protons by a force called electro-osmotic drag [30]. Additionally, water may diffuse through the membrane due to the concentration differences.

In the present study, the membrane water diffusivity and membrane ionic conductivity were calculated by the expressions given by Springer et al. [36]. It is almost a standard model that has been well explained in the recent textbook [37].

2.4. Volume-of-fluid (VOF) model

The VOF technique was implemented in the channels and porous media (including GDLs and catalyst layers) [33]. Interface between gas and liquid (two-phase flow) is tracked by the volume fraction of liquid water in the computational cell volume. In the VOF approach, the source term of continuity and momentum equations used in porous media include the effects of surface tension and wall adhesion and capillary water transport phenomenon, therefore, was also considered.

2.4.1. Geometric reconstruction scheme

The geometric reconstruction PLIC scheme (piecewise linear interface construction) was employed because of its accuracy and applicability for general unstructured meshes, compared to other methods such as the donor–acceptor, Euler explicit, and implicit schemes. A VOF geometric reconstruction scheme is divided into two parts: a reconstruction step and a propagation step. Details can be found in Refs. [33,38].

2.4.2. Implementation of surface tension

The addition of surface tension to the VOF method is modeled by a source term in the momentum equation. The pressure drop across the surface depends upon the surface tension coefficient χ [33,38]:

$$\Delta p = \chi\left(\frac{1}{R_1} + \frac{1}{R_2}\right) \tag{26}$$

where R_1 and R_2 are the two radii, in orthogonal directions, to measure the surface curvature.

The surface tension can be written in terms of the pressure jump across the interface, which is expressed as a volumetric force F added to the momentum equation:

$$\vec{F} = \chi\kappa\frac{\rho\nabla s_l}{(\rho_l + \rho_g)/2} \tag{27}$$

where χ denotes the surface tension coefficient and κ is the surface curvature. The source terms for different regions of the fuel cell are given in Table 2.

The surface curvature κ in Eq. (27) can be defined in terms of the divergence of the normal unit vector of the interface $\hat{n}$:

$$\kappa = \nabla \cdot \hat{n} = \nabla \cdot (\hat{n}_w \cos\theta_w + \hat{t}_w \sin\theta_w) \tag{28}$$

where $\hat{n}$ is the unit vector normal to the interface between two phases near the walls, $\hat{n}_w$ is the unit vector normal to the walls, $\hat{t}_w$ is the unit vector tangential to the walls, and θ_w is the static contact angle at the walls shown in Fig. 2. For the electrode surfaces with different wettabilities, different static contact angles were assigned, and different contact angles could result in different surface ten-

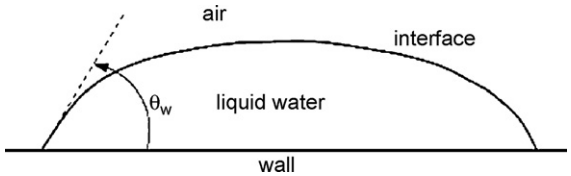

Fig. 2. Static contact angle at the walls.

sions (F), thus influencing on water transport. The values of surface tension and contact angle used in this model are listed in Table 1.

2.5. Mass transfer

Liquid water is considered to appear in the fuel cell when the water vapor pressure reaches its saturated value at the cell operating temperature. Contrarily, liquid water is evaporated when the water vapor pressure is smaller than its saturated value. Water condensation and evaporation phase change is also an important factor to determine the presence of liquid water in multi-phase model. In the present study, the variation of water mass flow rate was due to condensation (or evaporation) as described here [33]:

$$\dot{m} = r_{\mathrm{w}} \frac{M_{\mathrm{H_2O}}(P_{\mathrm{w}} - P_{\mathrm{sat}})}{RT} \tag{29}$$

2.6. Boundary conditions

To close the equation systems including conservation equations of continuity, momentum, energy, species, and charge with unknowns: u, v, w, p, T, Y_i and ϕ, the boundary conditions are required. The summary of boundary conditions is listed in Table 3. Below a brief description is provided.

2.6.1. Inlet of flow channels

Inlet velocities, fuel and oxidant temperatures and mass concentration of species were set as given parameters listed in Table 3. Inlet velocities can be preliminarily calculated by the inlet flow rates based on the average current density (I_{avg}) and excess coefficient ω that is defined as

$$\omega_{\mathrm{H_2}} = \frac{m_{\mathrm{H_2,supply}}}{m_{\mathrm{H_2,consumption}}}; \qquad \omega_{\mathrm{O_2}} = \frac{m_{\mathrm{O_2,supply}}}{m_{\mathrm{O_2,consumption}}} \tag{30}$$

Then, inlet velocity expression is given by the following equations:

$$U_{\mathrm{H_2,in}} = \omega_{\mathrm{H_2}} M_{\mathrm{H_2}} \frac{I_{\mathrm{ave}} A_{\mathrm{surf}}}{2F\rho_{\mathrm{H_2}} A_{\mathrm{in}}} \tag{31}$$

Table 3
Boundary conditions

Locations of application	Boundary conditions
Inlet of the anode flow channel	$u = U_{\mathrm{an,in}}$; $Y_{\mathrm{H_2}} = Y_{\mathrm{H_2,in}}$; $Y_{\mathrm{H_2O}} = Y_{\mathrm{H_2O,an,in}}$; $T_{\mathrm{an,in}} = T_{\mathrm{H_2,in}}$
Inlet of the cathode flow channel	$u = U_{\mathrm{cat,in}}$; $Y_{\mathrm{O_2}} = Y_{\mathrm{O_2,in}}$; $Y_{\mathrm{H_2O}} = Y_{\mathrm{H_2O,cat,in}}$; $T_{\mathrm{cat,in}} = T_{\mathrm{air/O_2,in}}$
Outlet of the anode flow channel	$\frac{\partial u_{\mathrm{out,an}}}{\partial x} = 0$; $\frac{\partial Y_{\mathrm{H_2}}}{\partial x} = 0$; $\frac{\partial Y_{\mathrm{H_2O,an}}}{\partial x} = 0$; $\frac{\partial T_{\mathrm{an,out}}}{\partial x} = 0$
Outlet of the cathode flow channel	$\frac{\partial u_{\mathrm{out,cat}}}{\partial x} = 0$; $\frac{\partial Y_{\mathrm{O_2}}}{\partial x} = 0$; $\frac{\partial Y_{\mathrm{H_2O,cat}}}{\partial x} = 0$; $\frac{\partial T_{\mathrm{cat,out}}}{\partial x} = 0$
The anode terminal	$\phi_{\mathrm{s}} = 0$; $\frac{\partial \phi_{\mathrm{m}}}{\partial y} = 0$
The cathode terminal	$\phi_{\mathrm{s}} = V_{\mathrm{cell}}$; $\frac{\partial \phi_{\mathrm{m}}}{\partial y} = 0$
External boundaries	$\frac{\partial \phi_{\mathrm{s}}}{\partial x} = 0$; $\frac{\partial \phi_{\mathrm{s}}}{\partial z} = 0$; $\frac{\partial \phi_{\mathrm{m}}}{\partial x} = 0$; $\frac{\partial \phi_{\mathrm{m}}}{\partial z} = 0$

$$U_{\mathrm{O_2,in}} = \omega_{\mathrm{O_2}} M_{\mathrm{O_2}} \frac{I_{\mathrm{ave}} A_{\mathrm{surf}}}{4F\rho_{\mathrm{O_2}} A_{\mathrm{in}}} \tag{32}$$

2.6.2. Outlet of flow channels

The fully developed condition was assumed to be applied for velocity field and species concentrations.

2.6.3. The terminal collectors

There were two terminal collectors in which the anode and cathode collectors were connected to the external electric circuit. It was necessary to determine the boundary conditions for phase potentials on these interfaces.

2.6.4. External boundaries

External boundaries are defined as all outside surfaces of PEMFC except the terminals (the outside surfaces of current collectors where the current entry to or departure from). Zero-current-flux condition was applied for the external boundaries due to no currents coming or leaving.

For the sake of simplicity, the cooling channel was not included in the present model. However, it is necessary to control the cell temperature. Consequently, the heat transfer was assumed to take place between the all outside surfaces and the ambient environment by forced convection as shown:

$$\dot{Q}_{\mathrm{convection}} = hA_{\mathrm{s}}(T_{\mathrm{s}} - T_{\infty})(\mathrm{W}) \tag{33}$$

where h is the convection heat transfer coefficient ($\mathrm{W\,m^{-2}\,K^{-1}}$), A_{s} is heat transfer surface area ($\mathrm{m^2}$), T_{s} and T_{∞} are the temperatures of the surfaces and the free stream, respectively.

Noted, heat is produced when the fuel cell operates. For the case in which water finally ends in vapor form, this heat generation rate is defined as [39]:

$$\dot{Q}_{\mathrm{generated}} = I(1.25 - V_{\mathrm{cell}})(\mathrm{W}) \tag{34}$$

In order to ensure that the forced convection dissipates the heat converted from electricity, the following condition must be satisfied:

$$\dot{Q}_{\mathrm{convection}} = \dot{Q}_{\mathrm{generated}} \tag{35}$$

then the convective coefficient h was chosen as

$$h = \frac{I(1.25 - V_{\mathrm{cell}})}{A_{\mathrm{s}}(T_{\mathrm{s}} - T_{\infty})} \tag{36}$$

2.7. Solution procedure

The above-coupled set of governing equations and relative equations were implemented into FLUENT® 6.2 by developing our own user-defined-functions (UDFs) based on the general FLUENT® package that does not include the PEMFC module developed by Fluent Inc. The developed own UDFs are written in C language with about 2000 statements. There were totally 279,500 grid cells in the computation domain used to simulate the physical and electrochemical phenomena in the fuel cell. The solution procedure for pressure–velocity coupling was based on PISO algorithm [40].

In order to save the calculation time, an unsteady single-phase model was simulated from the time $t = 0$ s to 0.5 s. At the time $t = 0.5$ s, an initialization of a series of liquid water droplets was initially suspended on the cathode channel at the time $t = 0.50$ s and a general model of PEMFC was called to further investigate two-phase flow behavior, especially liquid water behavior across porous media, together with electrochemical reaction, heat and mass transfer.

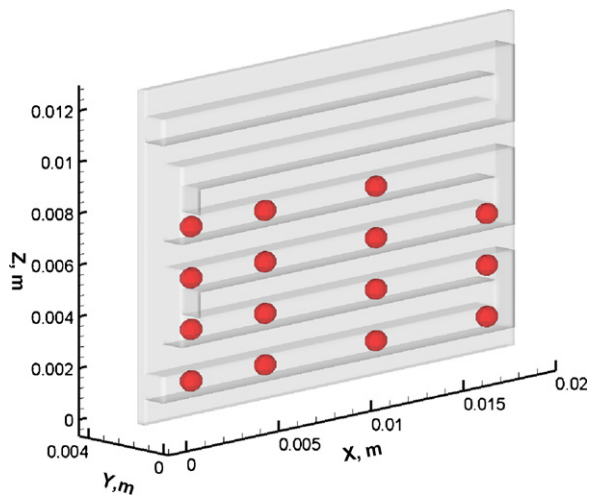

Fig. 3. A series of water droplets was initially suspended into the cathode channel.

3. Results and discussion

Fig. 3 shows the arrangement of the initial liquid water distribution. There were 15 equidistant spherical droplets ($r = 0.4$ mm) freely suspended along the cathode channel. The cell voltage was constantly set to be 0.5 V. The operating condition and fuel cell parameters are listed in Table 1.

3.1. Water distribution inside the fuel cell—comparison of numerical simulation and experimental visualization

Before we have comparisons, let us have a quick look at the experimental investigations in the available literature. Experimental studies to probe detailed liquid water transport from the GDL into the gas flow channels have been performed by Yang et al. [41] and Zhang et al. [42]. Three transparent PEMFCs with different flow fields, including parallel, interdigitated and cascade, were introduced by Liu et al. [43]. As presented in Liu's paper, the effects of flow field, cell temperature, cathode gas flow rate and operation time on water build-up and cell performance were presented, respectively. However, only the water flooding and two-phase flow in the transparent channel is visualized. Recently, there are some innovative visualization methods that were applied to investigate in situ the production and distribution of water in a PEMFC. Feindel et al. [44] developed a nuclear magnetic resonance (NMR) microscopy system to investigate the distribution of water throughout an operating H_2/O_2 PEMFC. The areas investigated include the flow fields, current collectors, membrane electrode assembly (MEA), and the membrane surrounding the catalysts. Another method is neutron radiography and tomography that has been successfully applied for investigation of liquid water evolution and transport in low temperature PEMFCs by Manke et al. [45] and Davey et al. [46].

Now let us make the comparisons. The water distribution in the channel and porous media of the fuel cell could be obtained from the numerical model. To validate the numerical results presented in this study, qualitative comparisons were made by using some available experimental visualization data. Fig. 4a presents the computed water distribution in a Y–Z cross-sectional plane of this fuel cell model. Fig. 4b depicts the water distribution captured by using Neutron Radiography method [46]. Note that in Fig. 4b, there was more water (black = no water; blue/white = more water) accumulated near the outlets than near the inlets. The water near the

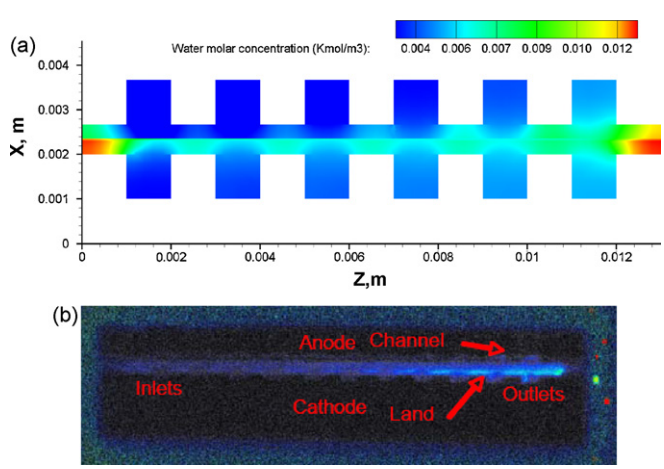

Fig. 4. (a) Water concentration distributions in the porous media on the cross-sectional planes (*Y–Z* plane) at $X = 0.01$ m; (b) water profile in two 2.25 cm^2 active area cells with 50% RH, 1.1 stoich and 172 kPa at the anode and 2.2 stoich and 172 kPa at the cathode at 1.4 A cm^{-2} and 100% RH at the cathode inlet (Davey et al. [46]).

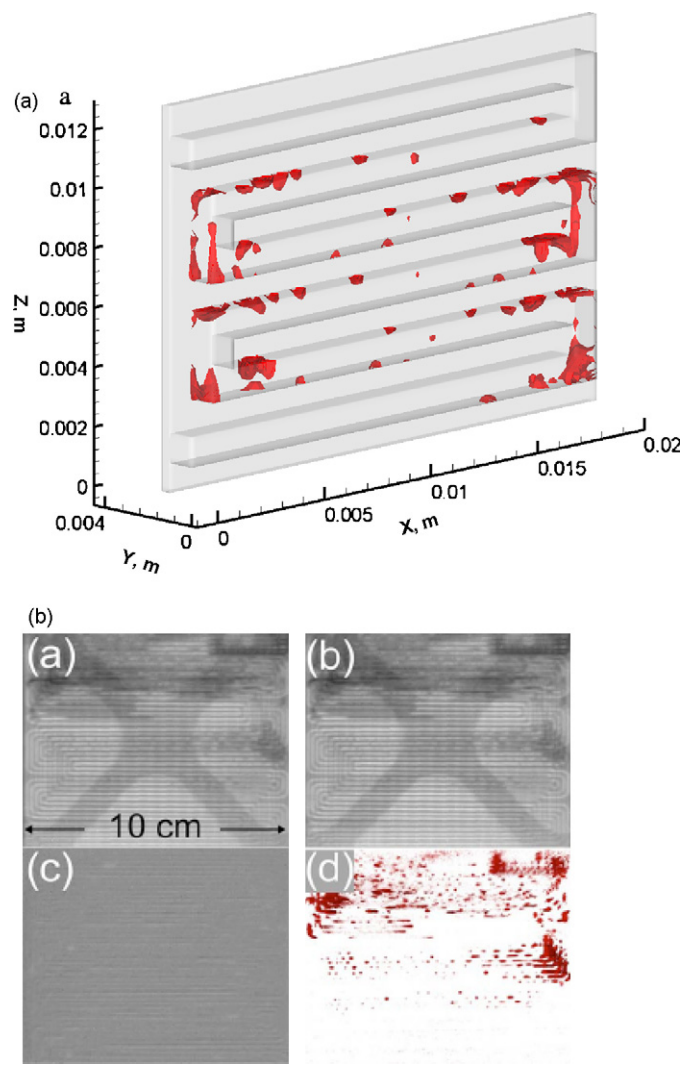

Fig. 5. (a) Volume fraction distribution of liquid water in the middle-plane of the cathode channel at $t = 0.502$ s; (b) neutron tomogram showing the three-dimensional water distribution in the cathode channel of a serpentine PEMFC (Manke et al. [45]): (b–a) right before shut up, (b–b) several hours after a tomography was performed, (b–c) quotient of image (b–a) and (b–b), (b–d) neutron tomogram showing the three-dimensional water distribution.

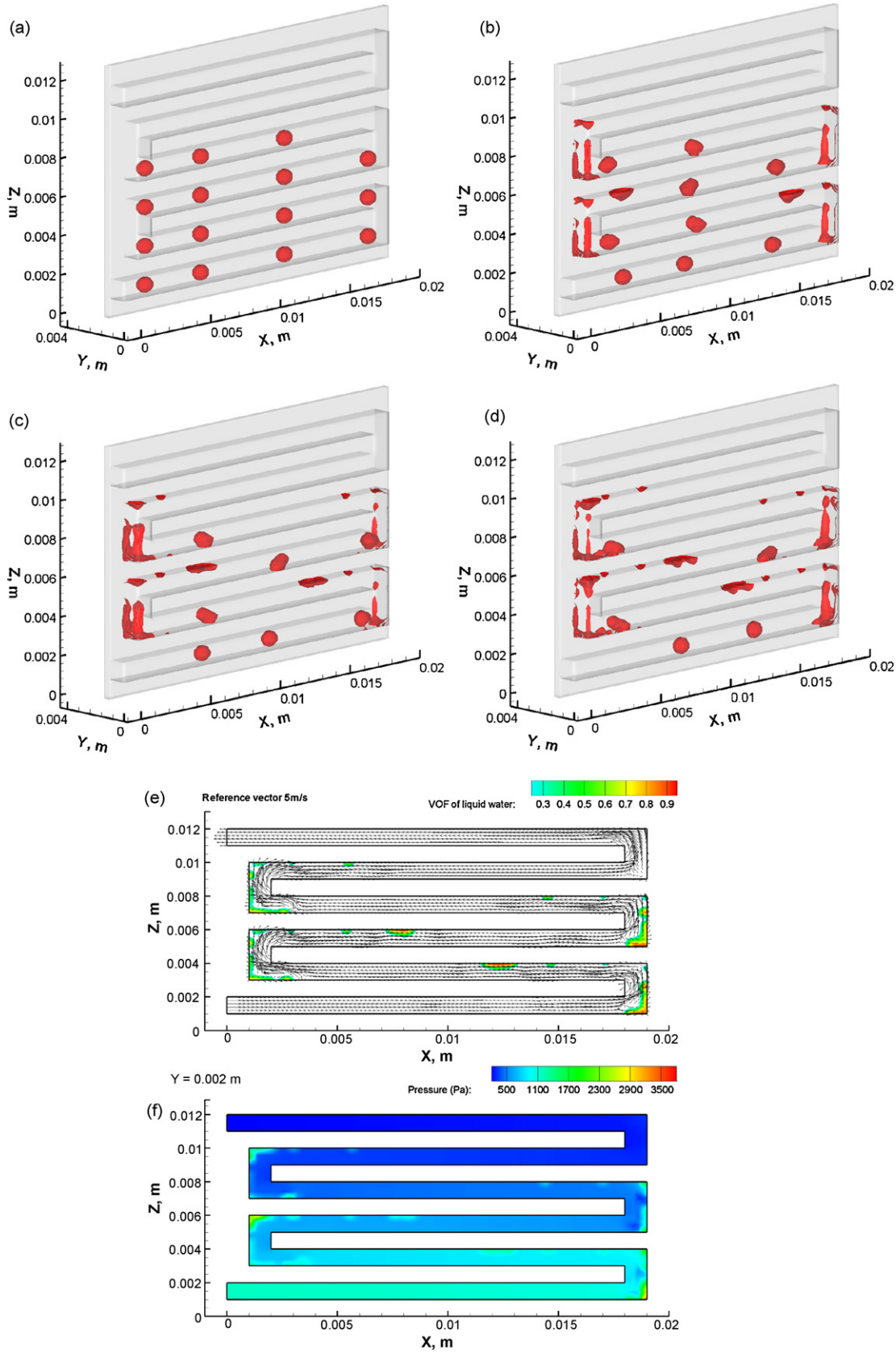

Fig. 6. The motion and deformation of droplets vs. time on the cathode channel: (a) $t = 0.500$ s; (b) $t = 0.50025$ s; (c) $t = 0.5005$ s; (d) $t = 0.50075$ s; (e) the velocity distribution and the volume-of-fluid of liquid water in the X–Z plane at $Y = 0.002$ m at $t = 0.50075$ s; (f) the pressure distribution and the volume-of-fluid of liquid water in the X–Z plane at $Y = 0.002$ m at $t = 0.50075$ s; (g) the water and velocity distribution in the different cross-sections along the main flow direction at $t = 0.50075$ s, corresponding to (a) $X = 0.001$ m, (b) $X = 0.006$ m, (c) $X = 0.014$ m and (d) $X = 0.019$ m, respectively.

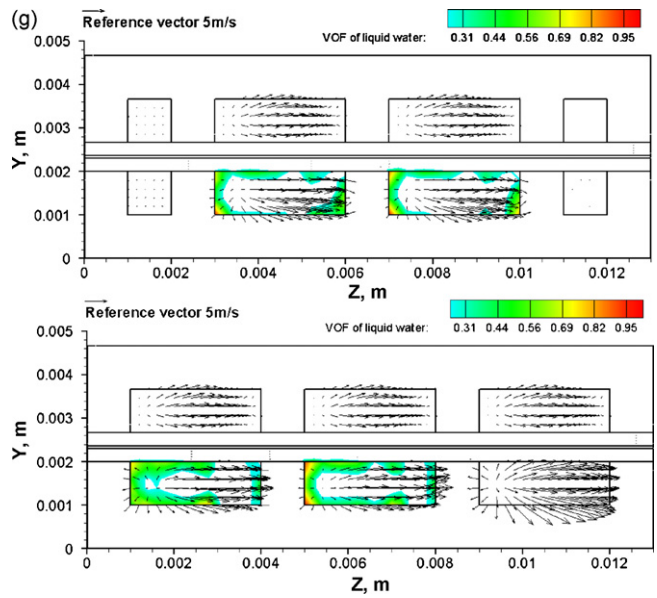

Fig. 6. (*Continued*).

outlet was more concentrated in the cathode GDL, especially the GDL above the land area. This is consistent with the generation of water at the cathode and its removal by the gas flow in the channels. The water generated above the land area needs to diffuse out laterally to the channel before it can be removed through the flow fields. The numerical result in Fig. 4a qualitatively shows good agreement with the experimental data in Fig. 4b made by Davey et al. [46]. In addition, more liquid water concentrated in the turning area of serpentine channel fuel cell is also presented by the computed model in this study shown in Fig. 5a and observed in Fig. 5b that was captured by using neutron tomography method in the experiments of Manke et al. [45].

In summary, by comparing the numerical results with available experimental results, we can conclude that the present general model is qualitatively in good agreement with the available experimental results. For this research, qualitative comparisons could not be conducted at the present time due to the sizes of the fuel cell in the cited experimental research are not known. The present authors are currently developing a bench experimental set-up to further validate the general model presented here and detailed results will be published in future.

3.2. The motion and deformation of liquid water inside the cathode channel

Fig. 6 shows the motion and deformation of droplets versus time on the cathode channel of the PEMFC. At $t = 0.5$ s, the droplet was placed at the channel inlet and was in its initial spherical shape (Fig. 6a). As time progressed, droplet deformation (elongation) in the flow direction, which is due to a combination of droplet surface tension and shear stress from surrounding airflow, could be observed. In other words, the enlargement of droplet surface area increased the surface tension such that the force balance on the droplet could be achieved. Fig. 6b indicates that, after hitting the turning surface, these deformed droplets had the tendency of fragmenting and then entering the central airflow due to the dragging effect from the turning flow. Obviously, in the turning area, the shear force from the airflow is much stronger than the droplet surface tension, thus together with the inertia force, resulting in significant droplet deformation and complex liquid water distribution. As the time progressed after milliseconds, the deformed droplets that enter the turning area from the straight channels hit the turning-wall surface. As a result, the deformed droplets were further elongated and the strong "turning" gas flow breaks these droplets into even smaller ones sticking on the turning-wall surface. Due to the effect of wall adhesion and surface tension, the smaller water droplets sticking on the turning-wall would slowly move forward while the other water droplets from the channel is continuously coming to the turning, and further broken into the other smaller ones. Such these water droplets would coalesce, then expanding and deforming into "water bands" due to the shear stress from "turning" gas flow and pressure drop, as shown in Fig. 6c and d. It is noted that since the coalescence of water droplets is formed in the turning area resulting in a high concentration of liquid water volume, a substantial blockage in the channel would take place. This blockage induces a decrease of the gap between the water droplets and the channel wall. In addition, the water droplets hitting the turning wall would stick onto it due to the wall adhesion. Fig. 6e shows the velocity distribution and the volume fraction of liquid water in the X–Z plane at $Y = 0.002$ m at $t = 0.50075$ s. The velocity field of airflow is accelerated through the gaps that were formed by the blockage of liquid water in the turning area, and then is decelerated after leaving the turning area in which the blockage occurs. In the other views shown in Fig. 6g, one can see that the water droplets hit the turning wall and expanded to the surroundings of the landing points. The droplets could induce high-pressure zones in the channel, as shown in Fig. 6f, especially in the turning area.

As the time progressed to $t = 0.501$ s, as shown in Fig. 7a, the water bands in the turning walls keep moving forwards along the main flow direction. One can see in Fig. 7a and b that, the water bands have a tendency of elongating without breaking away under the impact of shear force from the gas flow. However, the water bands were broken again into smaller droplets distributed over the straight channel wall since these bands left the turning area. Subsequently, the formed small water drops are easily removed and distributed everywhere on the straight channel walls, as it can be seen in Fig. 7c and d at $t = 0.504$ s and 0.506 s. Fig. 7e shows that the airflow is rapidly accelerated at the turning area due to the water blockage as earlier mentioned. Hence, the shear stress from the airflow in the straight channel is significant to break the water bands into small, discrete liquid droplets rather than deforming or elongating such water bands. This also results

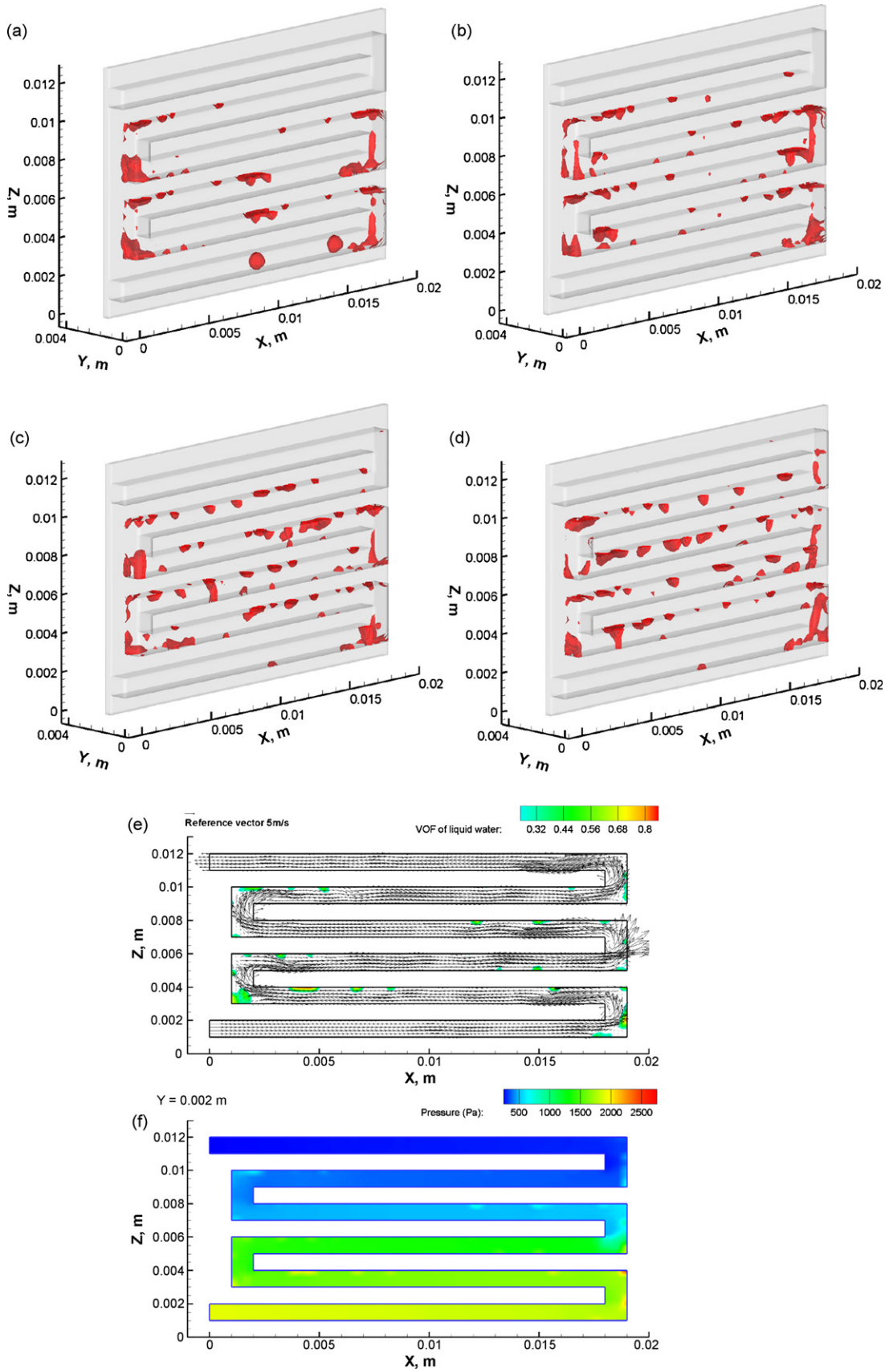

Fig. 7. The motion and deformation of droplets vs. time on the cathode channel: (a) $t = 0.501$ s; (b) $t = 0.502$ s; (c) $t = 0.504$ s; (d) $t = 0.506$ s; (e) the velocity distribution and the volume-of-fluid of liquid water in the X–Z plane at $Y = 0.002$ m at $t = 0.506$ s; (f) the pressure distribution and the volume-of-fluid of liquid water in the X–Z plane at $Y = 0.002$ m at $t = 0.506$ s.

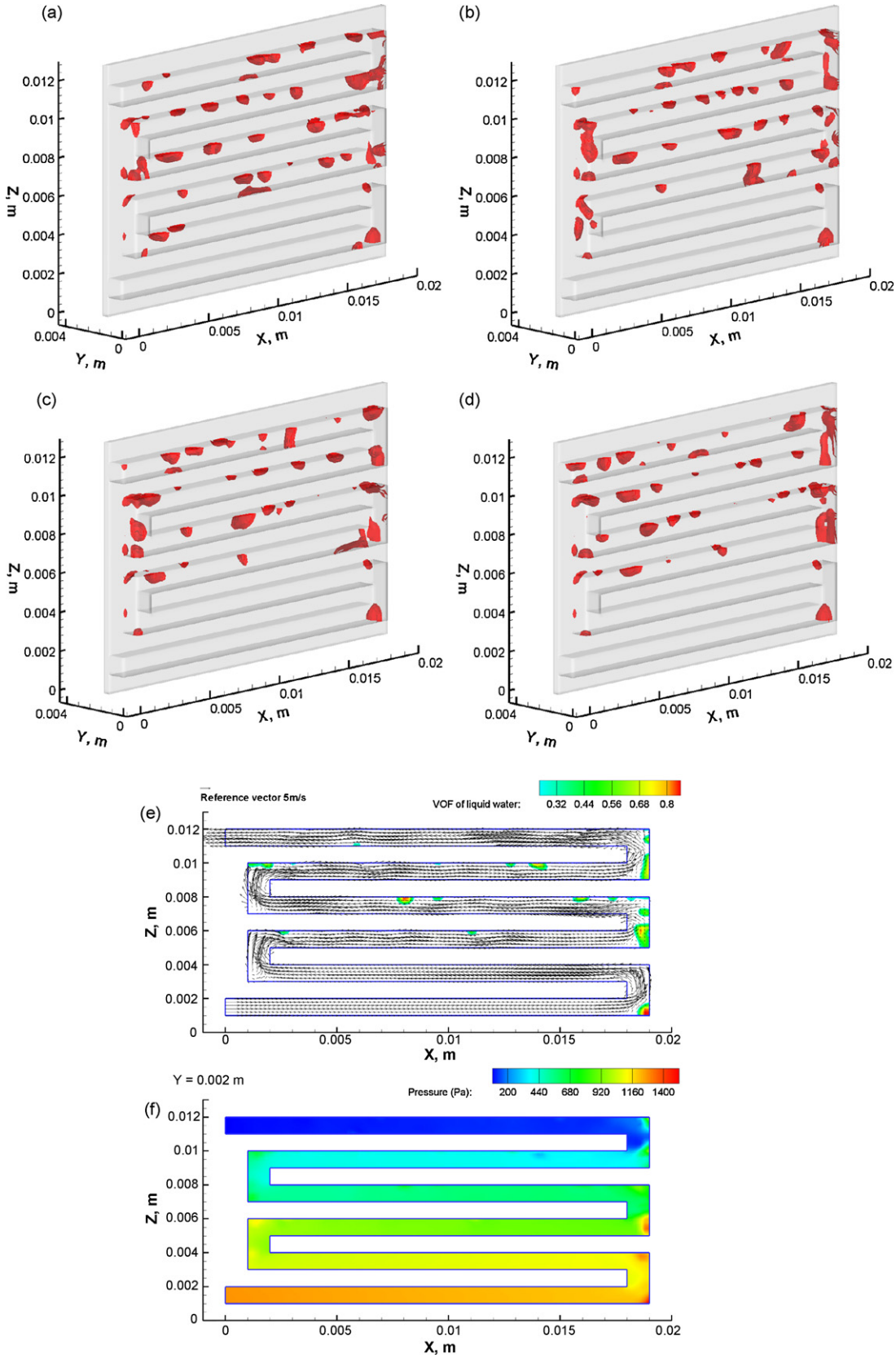

Fig. 8. The motion and deformation of droplets vs. time on the cathode channel: (a) $t = 0.520$ s; (b) $t = 0.522$ s; (c) $t = 0.524$ s; (d) $t = 0.526$ s; (e) the velocity distribution and the volume-of-fluid of liquid water in the X–Z plane at $Y = 0.002$ m at $t = 0.526$ s; (f) the pressure distribution and the volume-of-fluid of liquid water in the X–Z plane at $Y = 0.002$ m at $t = 0.526$ s.

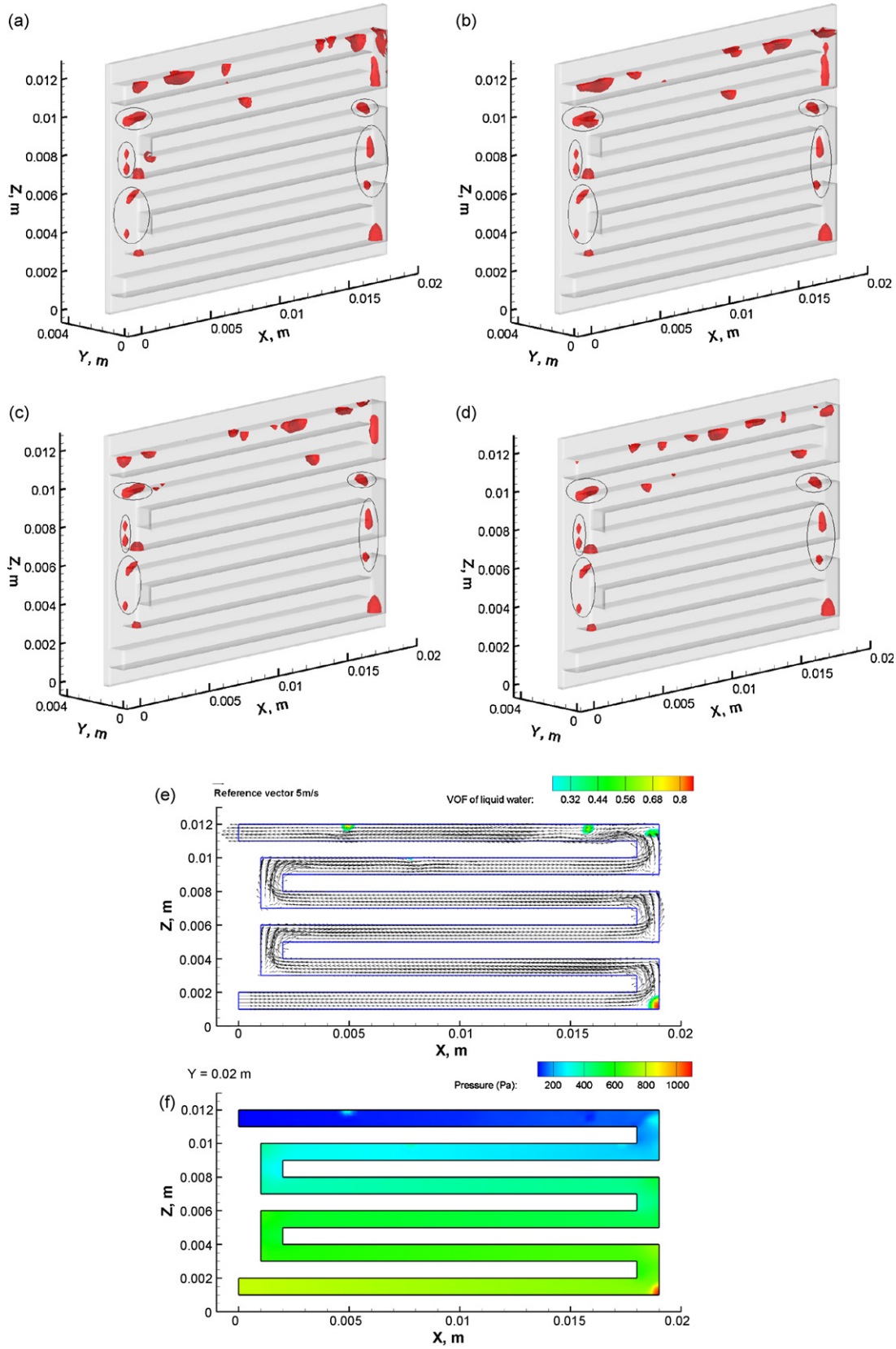

Fig. 9. The motion and deformation of droplets vs. time on the cathode channel: (a) $t = 0.560$ s; (b) $t = 0.562$ s; (c) $t = 0.564$ s; (d) $t = 0.566$ s; (e) the velocity distribution and the volume-of-fluid of liquid water in the X–Z plane at $Y = 0.002$ m at $t = 0.566$ s; (f) the pressure distribution and the volume-of-fluid of liquid water in the X–Z plane at $Y = 0.002$ m at $t = 0.566$ s; (g) the liquid water in the Y–Z plane at $X = 0.001$ m, 0.002 m, 0.018 m and 0.019 m.

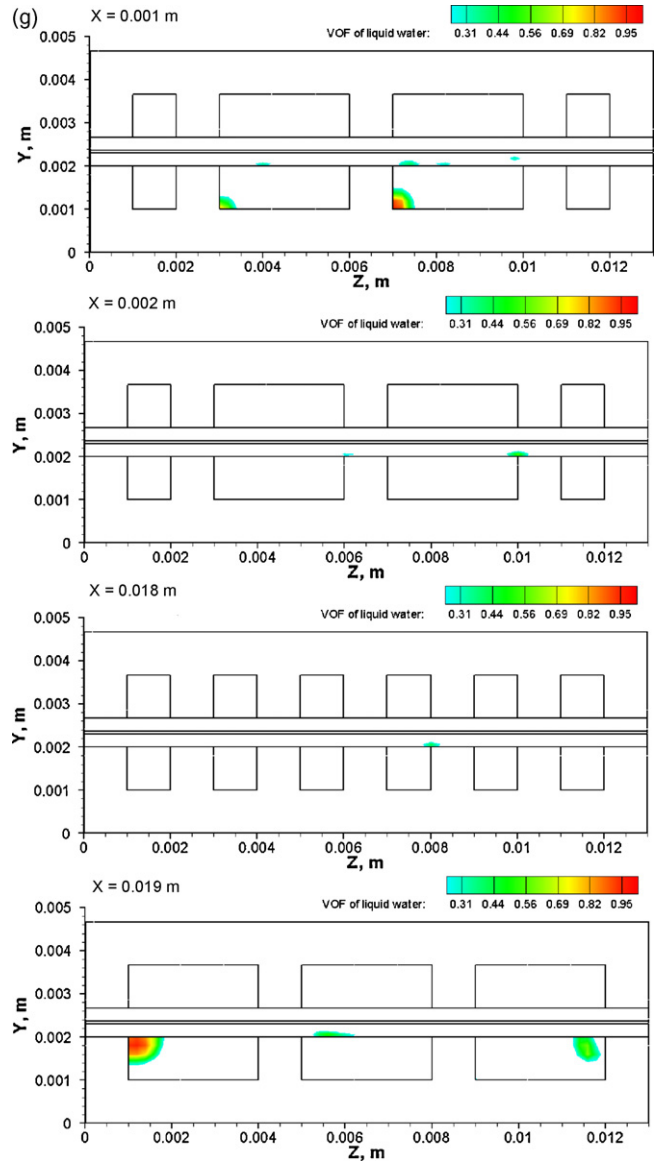

Fig. 9. (*Continued*).

in a decrease of pressure drop in comparison with the value at $t = 0.50075$ s.

At $t = 0.52$ s as shown in Fig. 8a, a portion of water droplets was removed from the cathode channel outlet by the gas flow. The small droplets tend to scatter everywhere in the channel rather than coalescing or forming water bands. Even in the turning area, it can be seen that the water bands either are tiny or are not formed at all. The wall adhesion of the small droplets previously coalesced at the turning areas is insufficient to resist the shear stress from the gas flow. In addition, one can see that there are some droplets penetrating to the gas diffusion layer. It can be realized that this phenomenon takes place mostly in the turning areas where the water is not easy to be removed rather than in the straight channel as previously discussed. As shown in Fig. 8b–d that as the time proceeds to $t = 0.526$ s, the water continues to be taken away from the channel outlet except the water amount remaining in the gas diffusion layer. At $t = 0.526$ s, as shown in Fig. 8e, the velocity field is observed to be "more stable" since a large amount of liquid water was taken away and then the blockage caused by the small droplets less influences on the gas flow movement. Consequently, this also results in an evident decrease in pressure drop distribution which is presented in Fig. 8f.

Most of the water droplets were moved out of the channel by the gas flow at $t = 0.56$ s. As the time proceeded to $t = 0.566$ s, it could be observed that there were only few small droplets remaining in the exit channel. However, an amount of liquid water penetrated through the gas diffusion layer seemed to be retained at the same position in the layer regardless the droplets in the channel continued to be removed outwards. It can be obviously seen that the water amount kept in the diffusion layer is marked by circles as shown in Fig. 9a–d. Noticeably, the marked circles in Fig. 9 evoke that the penetrated water usually occur in the turning area in which the liquid water is more difficult to be removed and have a tendency of passing through the gas diffusion layer instead of moving along the channel to the outlet. The liquid water in the gas diffusion layer is also clearly illustrated in Fig. 9g since the cross-sectional planes along X-direction at $X = 0.001$ m, 0.002 m, 0.018 m and 0.019 m are extracted. As time progresses, the more liquid water gradually move out of the channel, the less the liquid water blocks the flow field in the channel. Therefore, the block-

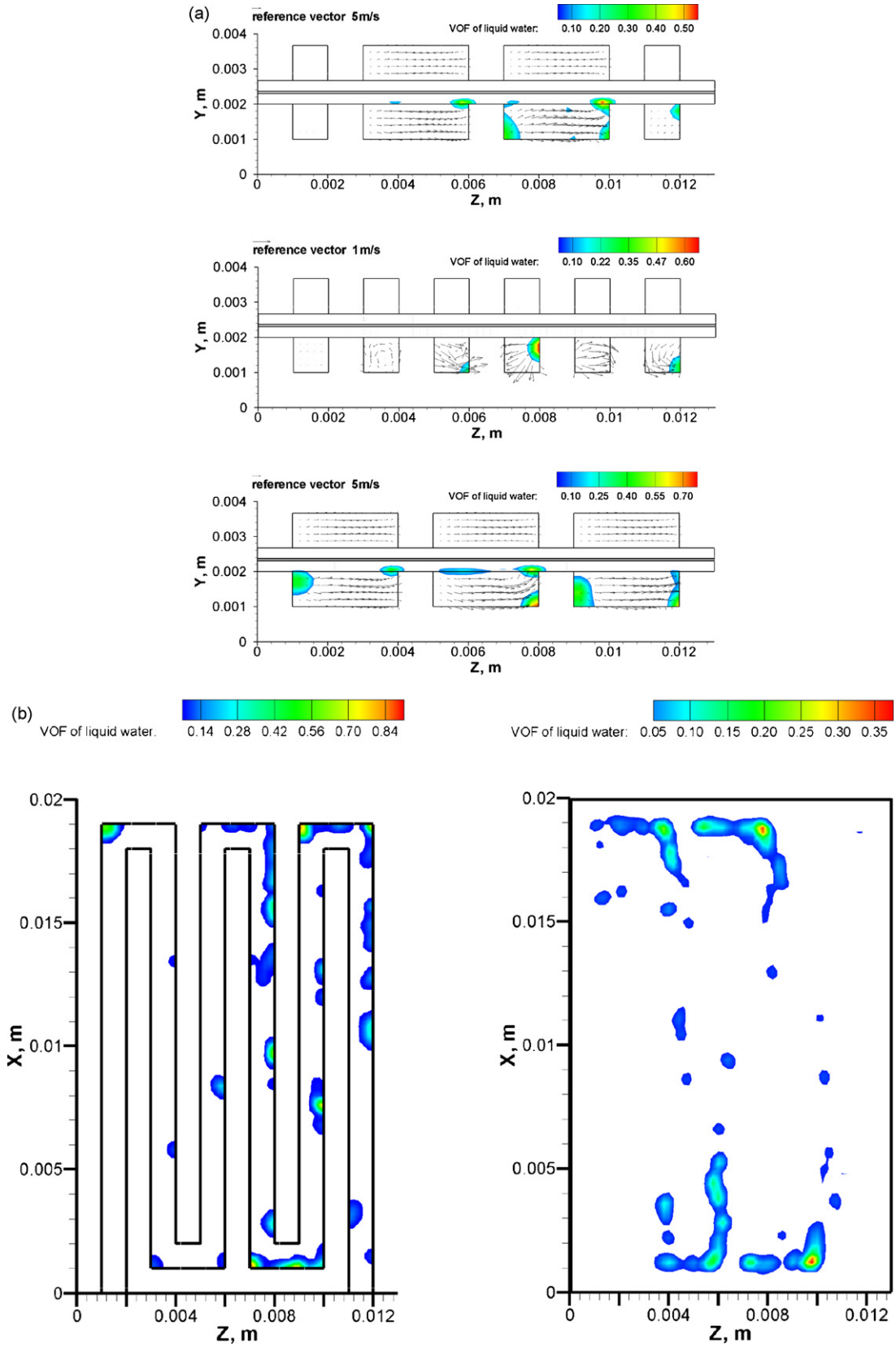

Fig. 10. (a) The distribution of volume fraction of liquid water in the cross-sectional planes (Y–Z plane) at $X = 0.0015$ m, 0.010 m and 0.0185 m (Case 2); (b) distribution of volume fraction of liquid water in the middle-plane of the cathode flow channel ($Y = 0.0015$ m) and catalyst layer ($Y = 0.002305$ m) (Case 2).

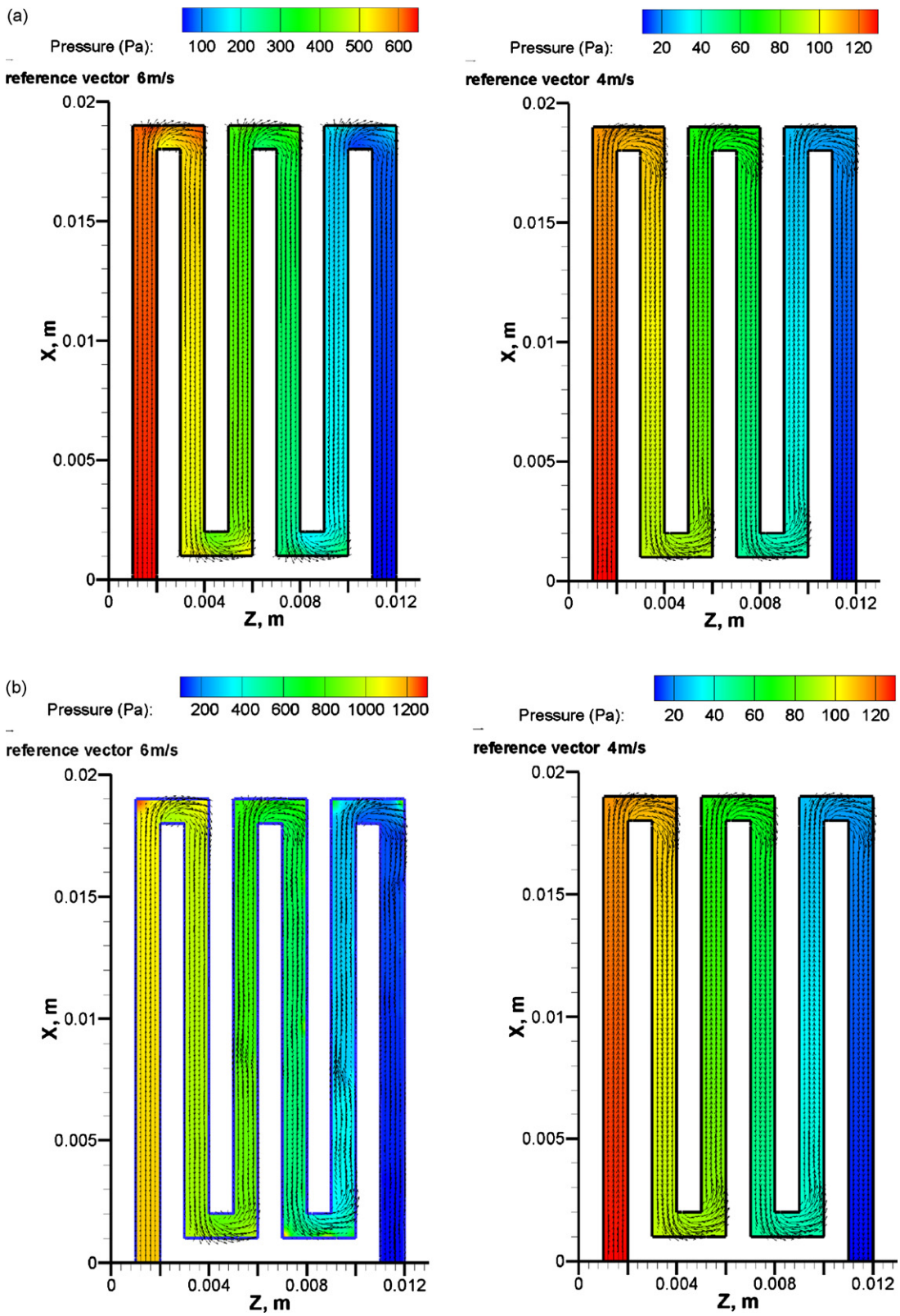

Fig. 11. Velocity vectors in the channel: on the middle-plane of cathode channel ($Y = 0.0015$ m) and the middle-plane of anode channel ($Y = 0.00317$ m): (a) Case 1 and (b) Case 2; on the cross-sectional planes (Y–Z plane) at $X = 0.0015$ m, 0.010 m and 0.0185 m: (c) Case 1 and (d) Case 2.

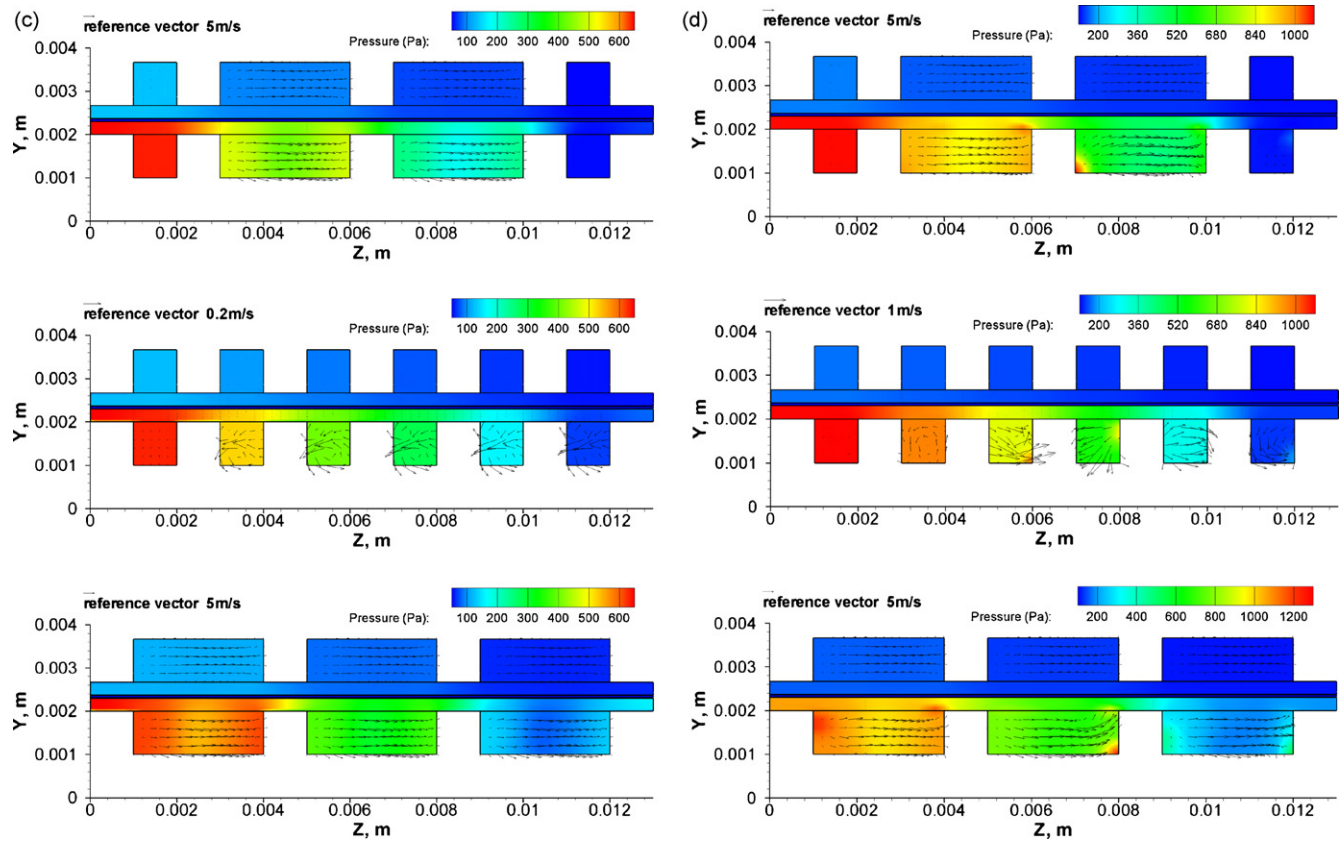

Fig. 11. (*Continued*).

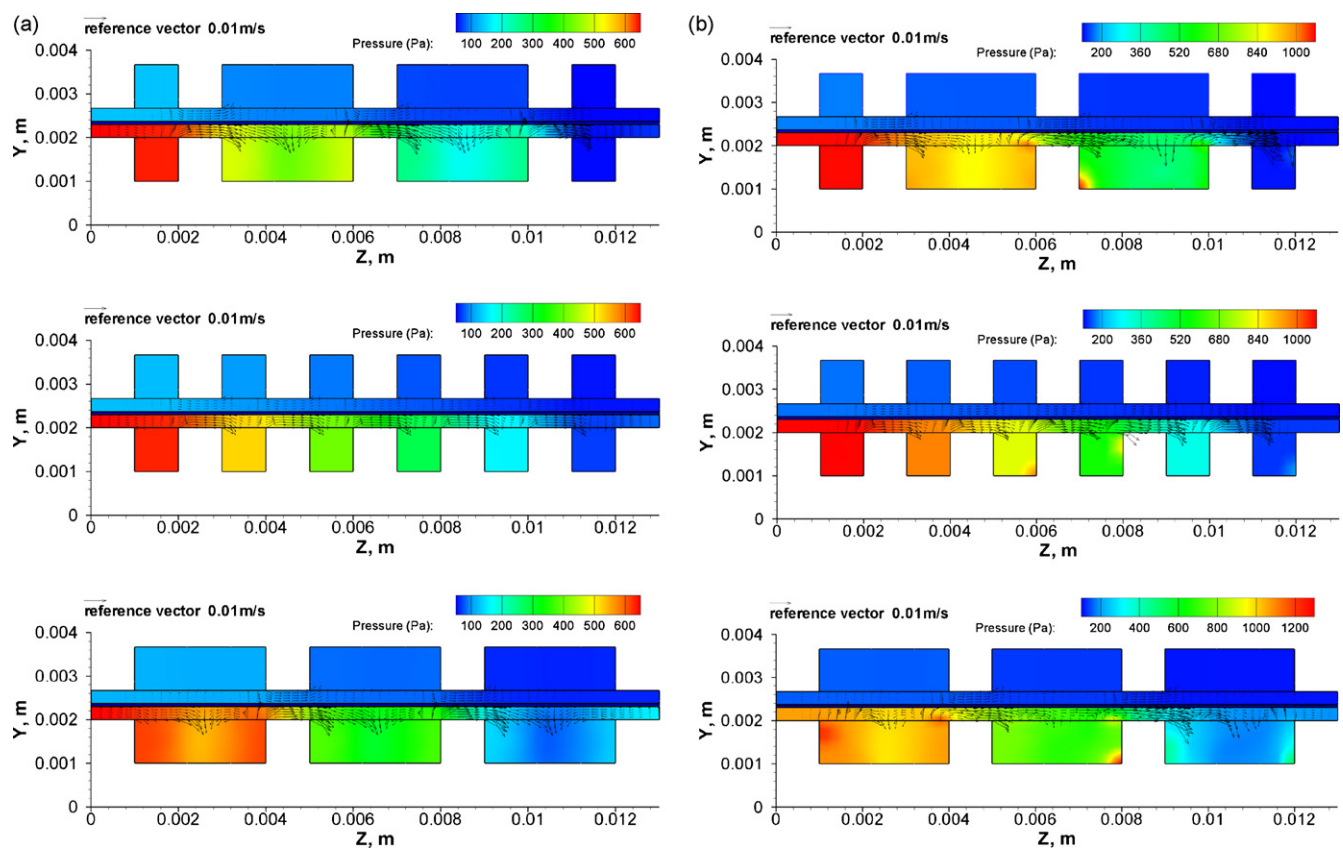

Fig. 12. Velocity vectors in the porous media on the cross-sectional planes (Y–Z plane) at $X = 0.0015$ m, 0.010 m and 0.0185 m: (a) Case 1 and (b) Case 2.

age insufficiently influences on the velocity and pressure fields in the fuel cell channel. It can be seen in Fig. 9e and f, the velocity and pressure fields at $t = 0.566$ s are more stable, have no sudden changes and have a smooth distribution along the channel, similar to those when compared with the case without liquid water in the channel.

3.3. Effects of liquid water on the fuel cell characteristics

In order to investigate the influences of liquid water on the cell characteristics and operating condition, two cases (Cases 1 and 2) are compared in this study. The first case would be considered at the time instant $t = 0.53$ s when the liquid droplets were not

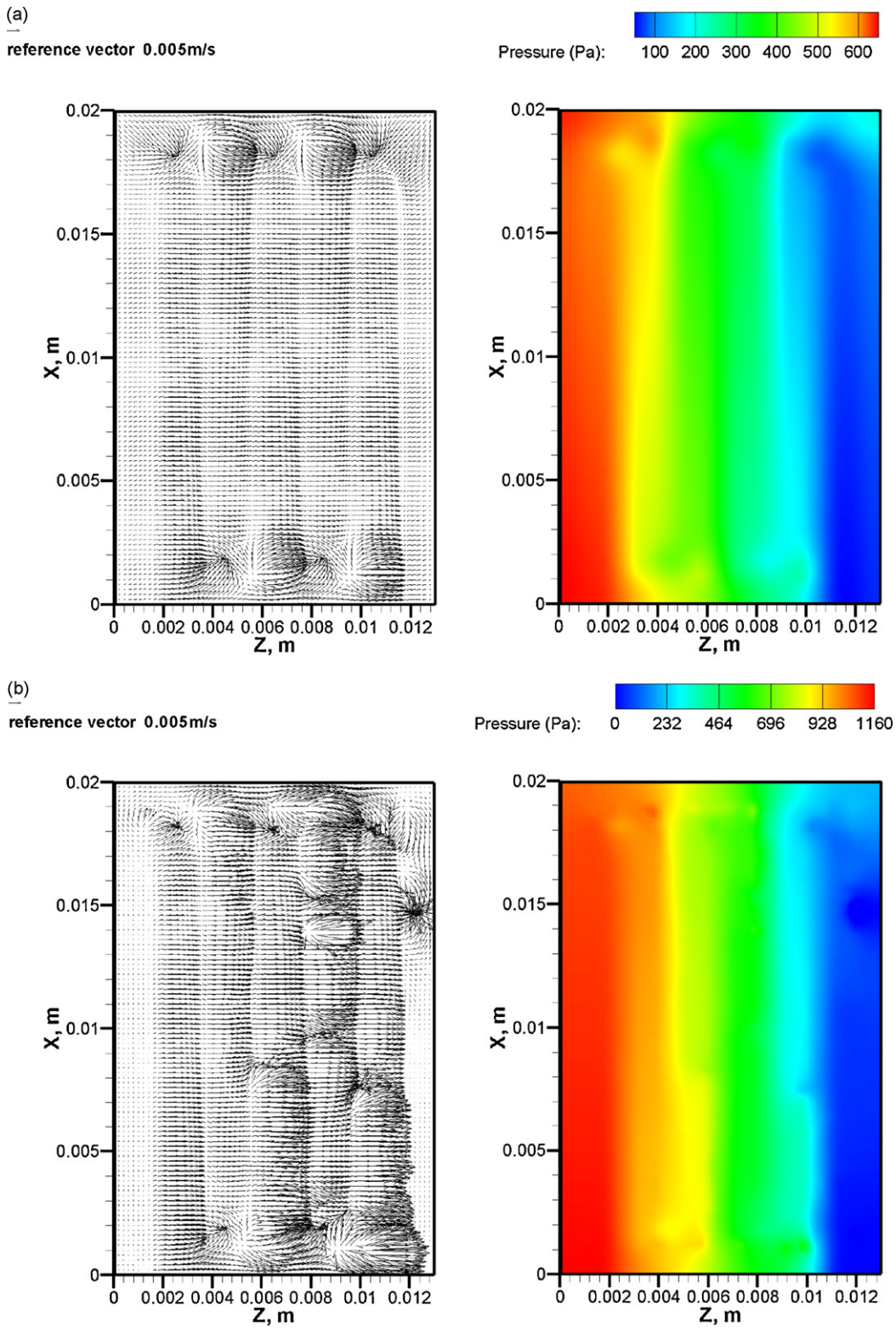

Fig. 13. Velocity vectors and pressure distributions on the middle-plane of catalyst layers (0.002305 m): (a) Case 1 and (b) Case 2.

introduced in the cathode channel and therefore the fuel cell operates in the condition without liquid water. The second case would be presented at the time instant $t = 0.53$ s since a series of water droplets had been introduced at $t = 0.5$ s into the cathode channel and evolved for 0.03 s that can be used to show the liquid water effects. In Case 2, fuel cell characteristics such as velocity, pressure, temperature, species concentrations and the fuel cell performance, etc. are considered as taking the appearance of water droplets into account. Hence, the numerical model at the first case was considered as single-phase model and the second case was considered

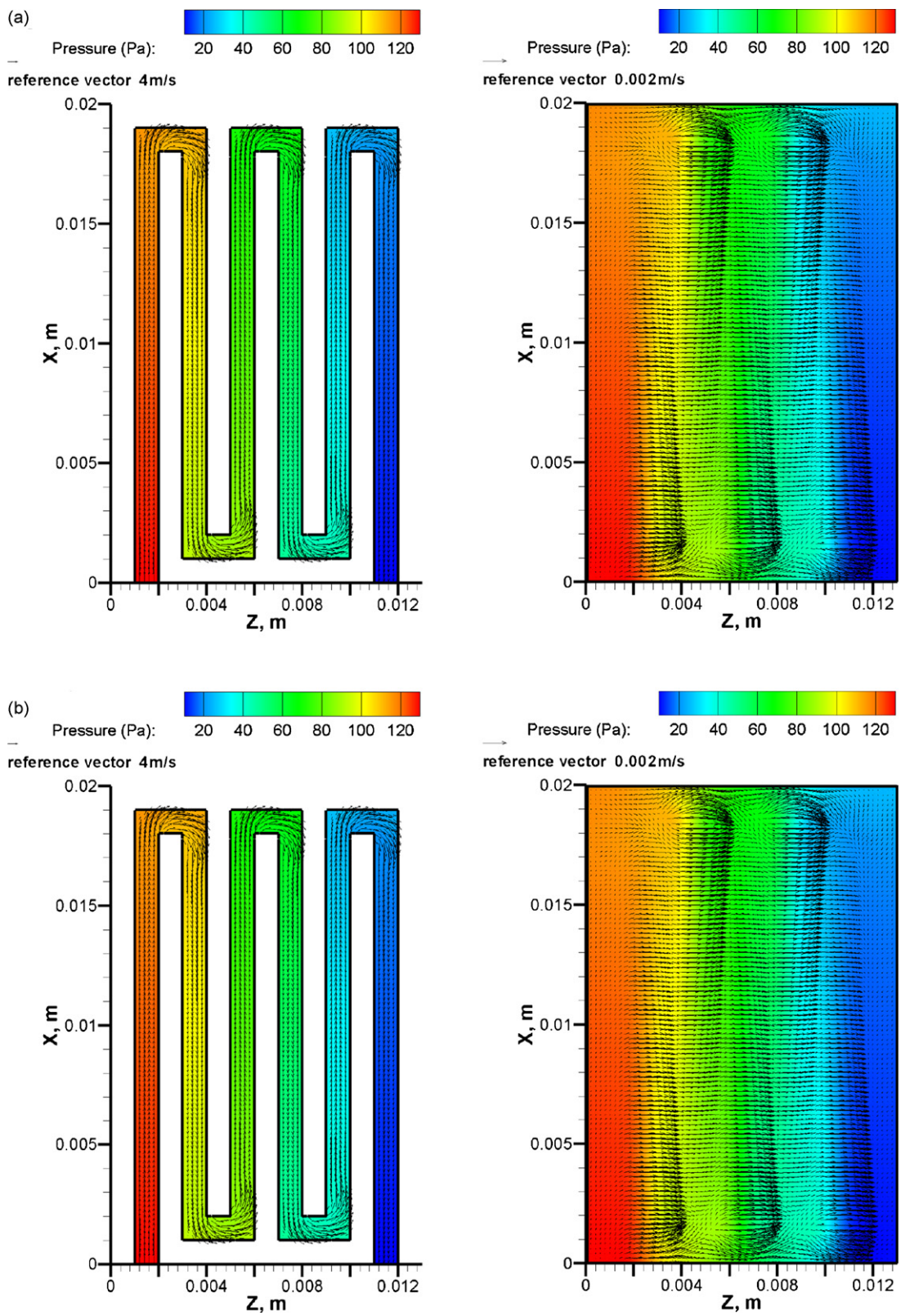

Fig. 14. Velocity vectors and pressure distributions on the middle-plane of anode channel ($Y = 0.00317$ m) and catalyst layers (0.002365 m): (a) Case 1 and (b) Case 2.

as the general model that includes two-phase interface tracking together with all other detailed sub-models.

3.3.1. Volume fraction of liquid water

In Case 2, Fig. 10a shows the distribution of volume fraction of liquid water in the cross-sectional planes (Y–Z plane) at $X = 0.0015$ m, 0.010 m and 0.0185 m and Fig. 10b depicts in the middle-plane of cathode flow channel and catalyst layer, respectively. Note that the liquid water was not taken into account in single-phase flow that was applied for the fuel cell prior to $t = 0.50$ s. Therefore, the presence of volume fraction of liquid (liquid water distribution) is not applicable to Case 1. It could be observed that

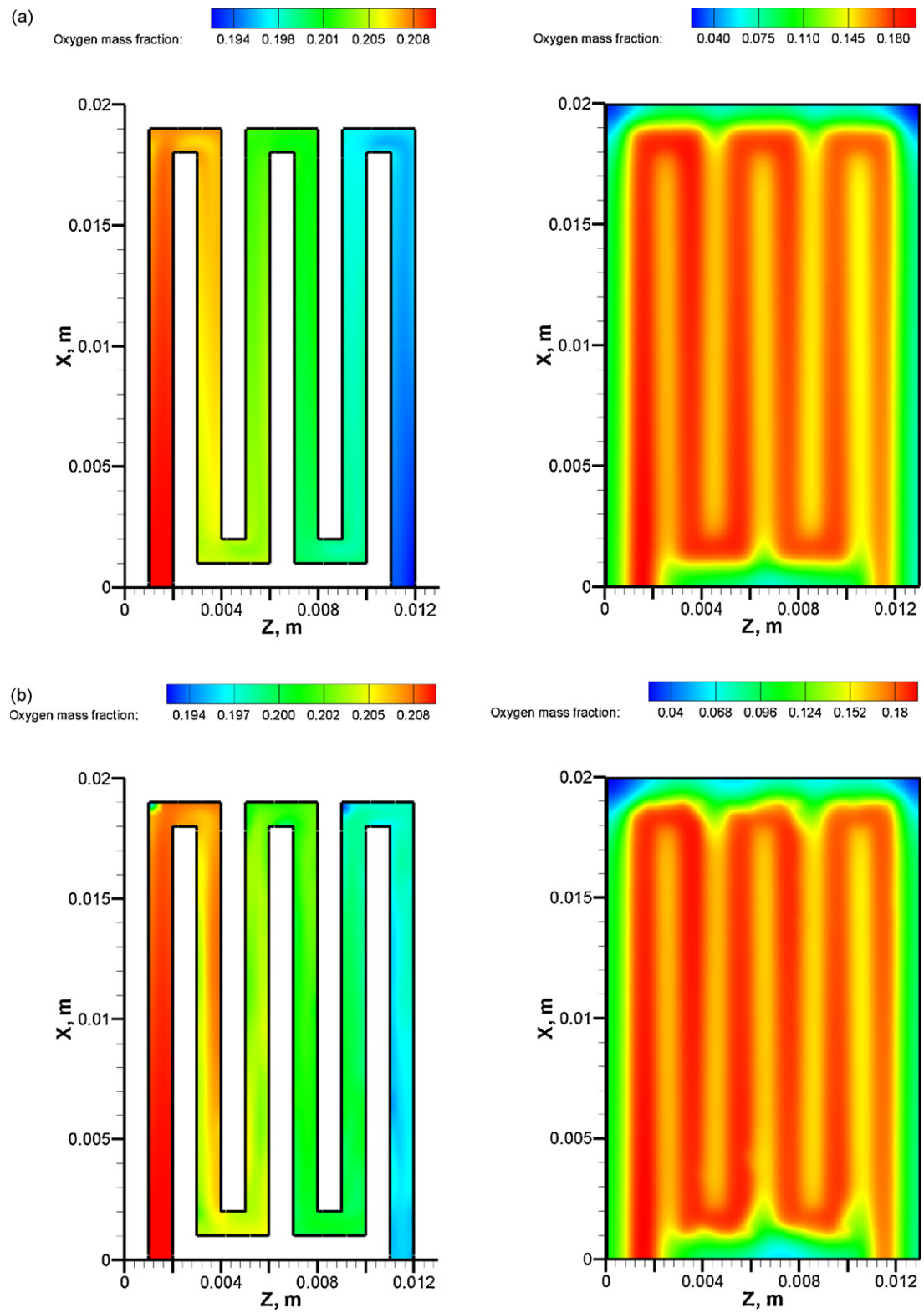

Fig. 15. Mass fraction distributions of oxygen on the middle-plane of cathode channel ($Y = 0.0015$ m) and catalyst layers (0.002305 m): (a) Case 1 and (b) Case 2.

the liquid droplets distributed in the fuel cell at a specified time were presented via volume fraction of water. To investigate the motion and interaction of liquid droplets inside the fuel cell and the influence of liquid phase on the fuel cell operating condition, the results of this simulation would be analyzed as the time progressed after 0.03 s at $t = 0.53$ s. The change of the water occupation fraction in the channel and liquid water transport from the cathode channel to the porous media were studied. By tracking the presence of volume fraction of water, one can determine where the liquid water occurs and the effects of presence of liquid water

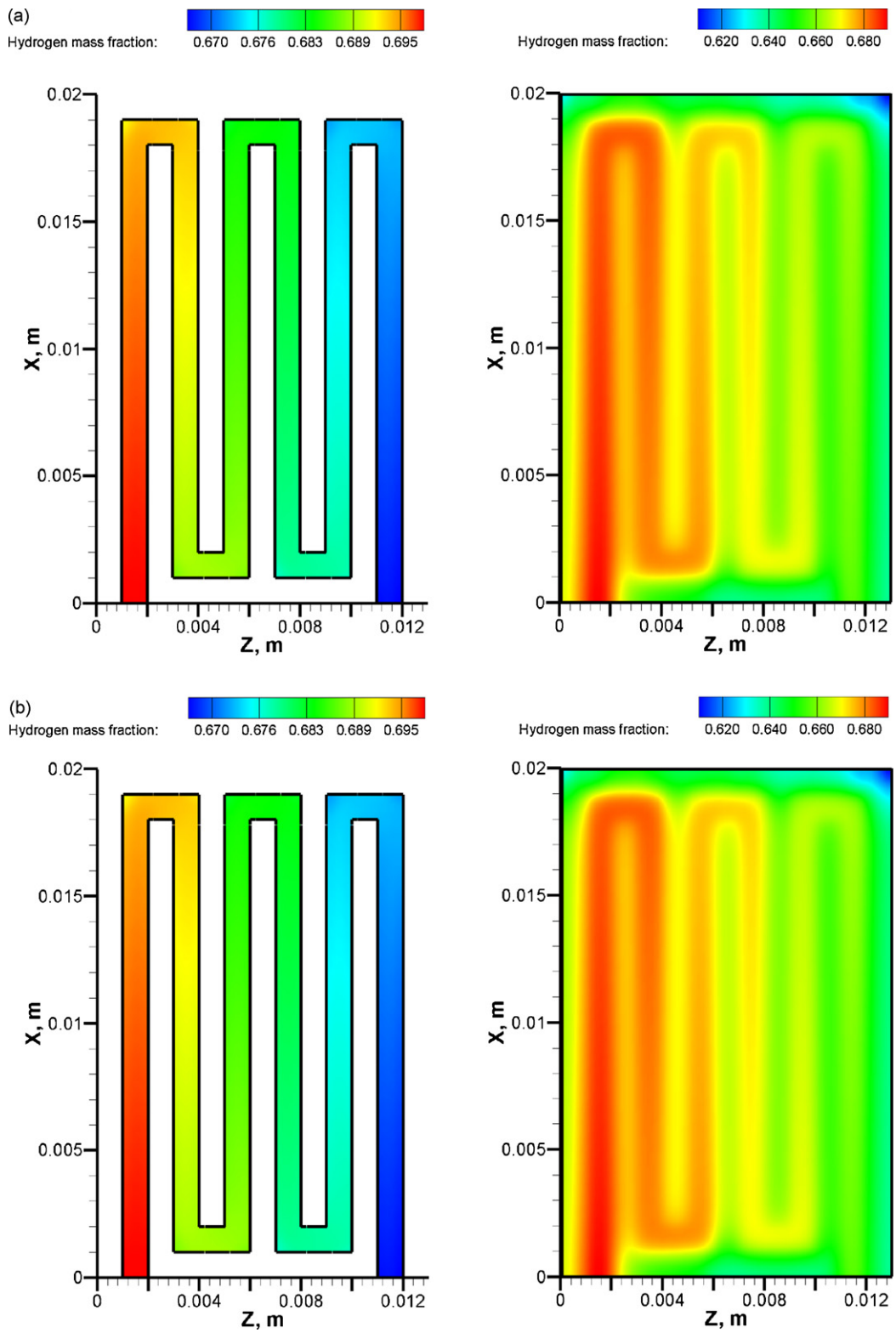

Fig. 16. Mass fraction distributions of hydrogen in the middle-planes of anode channel ($Y = 0.00317$ m) and catalyst layers (0.002365 m): (a) Case 1 and (b) Case 2.

on the physical parameters and characteristics of the fuel cell. Fig. 10a and b shows that most of the liquid water concentrated in the channel and moved through porous media is in the turning area of the serpentine-shaped flow channel. As a result, this would especially influence the other flow parameters of the turning area also.

3.3.2. Liquid water effects on velocity field and pressure distribution

The velocities at the cathode and anode inlets are 7.0 m s^{-1} and 4.5 m s^{-1}, respectively. Fig. 11a and b shows that the gases (air and water vapor at cathode; and hydrogen and water vapor at anode) are supplied from the inlet, moving along each branch of the

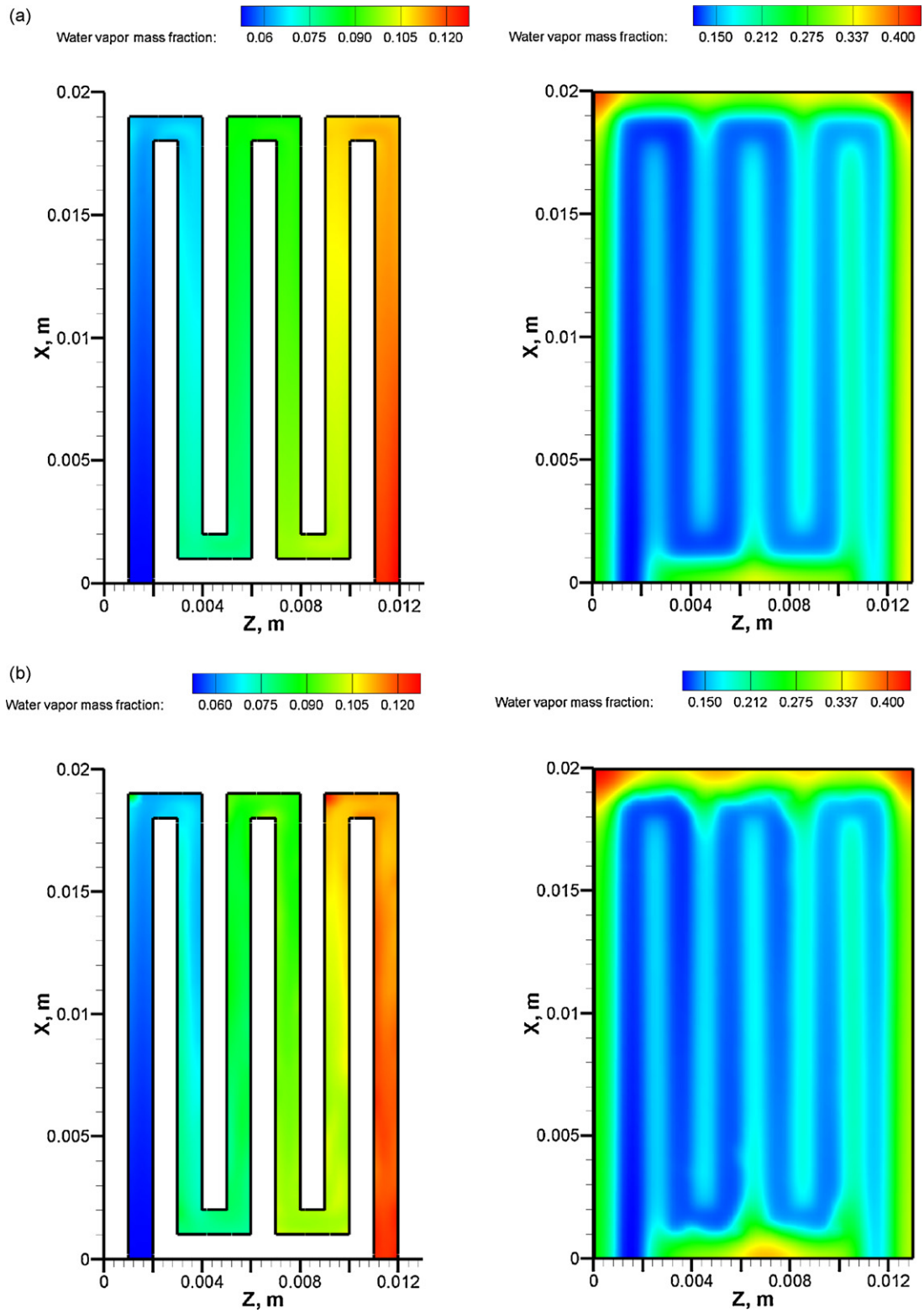

Fig. 17. Mass fraction distributions of water vapor on the middle-plane of cathode channel (Y = 0.0015 m) and catalyst layers (0.002305 m): (a) Case 1 and (b) Case 2.

serpentine-shaped channel for Case 1 and Case 2, respectively, dramatically varied their direction when approaching the turn, then go to the next branches. In Case 1 (Fig. 11c), the velocity vectors on *Y–Z* planes on cross-sectional planes of channel branches shown in Fig. 11c seem to have similar variation to each other. In other words, these velocity distributions on the same cross-section through all channel branches are the similar. This is because that liquid water was not considered in Case 1 and therefore there are no liquid droplets effects on the flow field. In Case 2 (Fig. 11d), the velocity and pressure distributions are quite different. Due to the presence and blockage of water droplets over the channel as previously mentioned, the flow field was not similar to each other depending on where the droplets located. It is noticeable that the pressure drop in Case 2 was observed to be higher than that in Case 1, especially around the location of the droplets, the pressure drop reaches highest values due to the momentum resistance caused by liquid water in airflow.

The velocity in the gas channels on both sides shown in Fig. 10a and b were very high (the order of magnitude is 1) by comparing to the low velocity in the porous media shown in Fig. 12a and b (the order of magnitude is 10^{-2}) due to the flow resistance in the porous media (including GDLs and catalyst layers). Although the porous media is solid, there still exists the flow field due to pressure gradient distribution in the void of such regions where reactant gases and water can move through. It can be seen in Fig. 12a and b for both cases that the flow in *Y–Z* planes had a tendency of moving through the porous media from one channel branch to the next, especially in the land area (the porous zones underneath the collector ribs). The difference of pressure on the same cross-section in all branches is the driving force to such flow motion. Similarly, it can be clearly seen in Fig. 12b how the blockage of liquid water in the porous media influenced the velocity fields. On the contrary, for the case where liquid water was absent in the fuel cell as shown in Fig. 12a, it is most likely that the flow in *Y–Z* planes in the porous media had no change on the same cross-section for every channel branch.

Fig. 13a and b shows velocity vectors and pressure distributions on the middle-plane of catalyst layers (0.002305 m) for Cases 1 and 2, respectively. Now, the flow field on *X–Z* planes could be observed. In both cases, there remained alternate velocity distributions having "triangle-shaped" on the porous media in which the magnitude of velocity vectors increased or decreased along the *X*-direction. This is the nature of fluid flow. It could be noticed that the high velocity vectors were located in the region in the land area between the two corners of two sequent branches, also having the largest pressure difference. The flow in the corner of a branch, therefore, tends to move towards the corner of the next branch at the same side through the porous media instead of moving along the channel. This is the shortest way and easiest way as well. The magnitude of such velocity vectors decreases along the channel due to the decrease of pressure difference and it is lowest at the corner at opposite side where the flow freely moves in the channel turn. Moreover, the chaos of velocity distribution caused by the effect of liquid water corresponding to the location of droplets in the porous media is more realized as shown in Fig. 13b.

Fig. 14a and b shows velocity vectors and pressure distributions on the middle-plane of anode channel ($Y = 0.00317$ m) and catalyst layers (0.002365 m) for Cases 1 and 2. Note that the flow field in the fuel cell may vary at the different times. Because the flow conditions at the anode side reached the steady state at Case 1 and the time period between Case 1 (at $t = 0.50$ s) and Case 2 (at $t = 0.53$ s) is almost negligible, then the velocity and pressure distributions were almost the same for the both cases due to the absence of liquid water at the anode side.

3.3.3. Liquid water effects on concentrations

In the both cases, it could be observed that the oxygen fraction decreased along the cathode channel from the inlet to the outlet

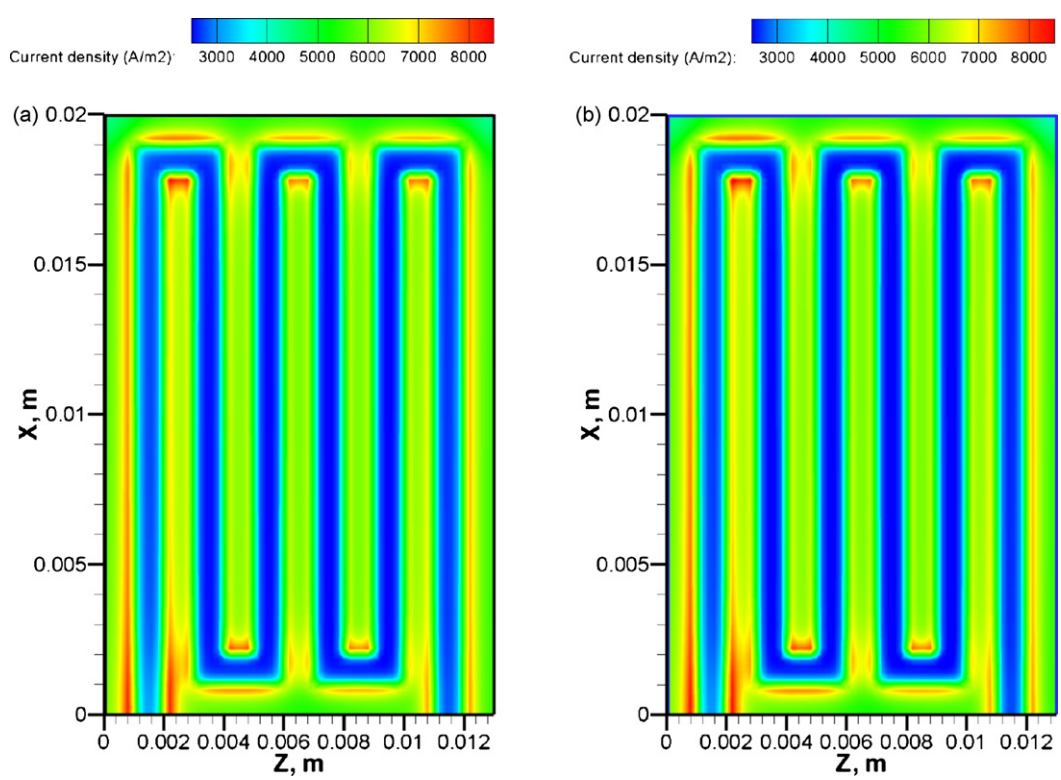

Fig. 18. The distribution of local current density at the catalyst/GDL interfaces at the cathode and anode: (a) Case 1 and (b) Case 2.

and from the channel to the catalyst layer due to the oxygen consumption on the catalyst layer. Mass transport of oxygen from the channel to the GDL was mainly driven by its concentration gradient (diffusion) and this effect was also partially influenced by the velocity component (convection) inside the porous media. The flow in cathode channel enhanced the gas transport in the region under the channel, rather than in the region under the rib (the land area). As shown in Fig. 15a and b, high oxygen region under the cathode channel was observed. On the other hand, the land area had a low amount of oxygen. There are two reasons accounting for this; the first is that mass transport of oxygen in such area was low due to weak influence of convection and diffusion. The second is that a large amount of oxygen was consumed due to a high reaction rate—the chemical reaction had strongly taken place in the land area which was directly connected to the collector ribs that the current density vectors mainly went through. This phenomenon will be discussed in later section. The presence of liquid water significantly influences the oxygen concentration in the channel and porous media as well. This is very important in water management of a fuel cell. As mentioned in many studies, liquid water occurring in the fuel cell causes the flooding phenomenon and further blocks the oxygen transport through the GDL and catalyst layer, then significantly influences the fuel cell performance. In Case 2, there was a noticeable blockage of liquid water in oxygen concentration, especially in the land region underneath the turning area. In Case 1, the oxygen mass fraction distribution in the porous media underneath the turning area could be seen to have a uniform, smooth U-shaped as shown in Fig. 15a. Differently in Case 2, the shape was various, unsmoothed and arbitrary. This is because the liquid water occupied the void in which oxygen was supposed to occupy. The higher volume fraction of liquid water occupies, the lower the oxygen mass fraction could be observed.

Similar to the oxygen mass fraction distribution in the cathode, the hydrogen gradually decreased from the inlet to the outlet in both the anode flow channel and porous media as shown in Fig. 16a and b. However, the decrease of hydrogen mass fraction along the anode channel was insignificant due to absence of liquid water.

For the both cases, the water vapor mass fraction increased along the cathode channel by two sources: by-product water was generated from the electrochemical reaction at the cathode and the migration of water from the anode to the cathode due to the electro-osmotic drag. As shown in Fig. 17 that there was a high water vapor content remaining in the land area at the cathode as a result of water build-up due to the higher reaction rate. Furthermore, due to the small velocity field in the land area nearby the edge (shown in Figs. 11 and 12), the accumulated water in such area was not easy to be removed. Obviously, water concentration is highest in the edge adjacent to the outlet channel branch due to water build-up and low convection effect. In Case 2, the presence of liquid droplets also influenced the distribution of water vapor mass fraction, similar to

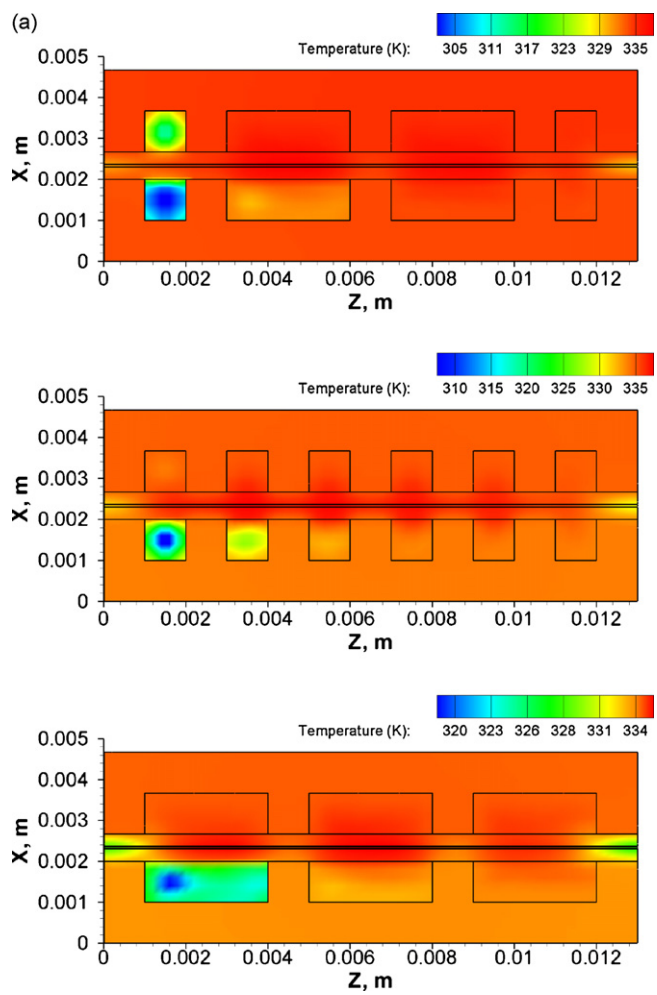

Fig. 19. (a) Temperature distribution in the cross-sectional planes (Y–Z plane) at X = 0.0015 m, 0.010 m and 0.0185 m (Case 2); temperature distributions on the middle-plane of cathode channel (Y = 0.0015 m) and catalyst layers (0.002305 m): (b) Case 1 and (c) Case 2.

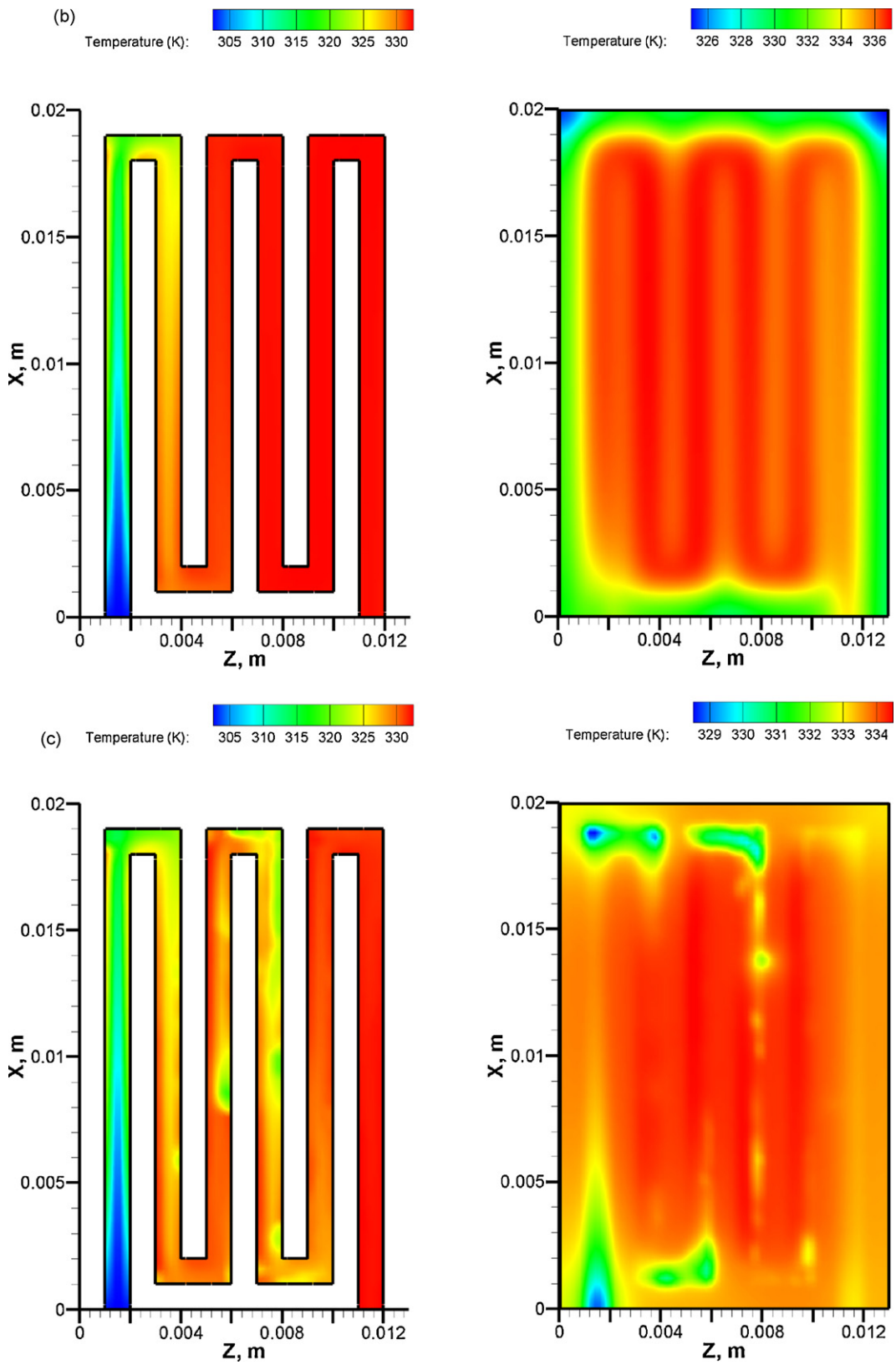

Fig. 19. (*Continued*).

that on oxygen transport. As can be seen in Fig. 17b, the higher the volume fraction of liquid water occupied, the larger the water vapor mass fraction observed.

3.3.4. Liquid water effects on current density distributions

Fig. 18a and b shows the distribution of local current density at the catalyst layer/GDL interfaces on the cathode and anode sides for the both cases, respectively. Note that the local current density at the interfaces was generated by the electron movement while the local current density at the mid-plane of the membrane by the proton movement through the membrane. The current density peaked at the land area in the porous media because the current flow tended to pass through the land area of GDLs/catalyst layers which were in direct contact with the collector ribs. Hence, the current flow could move through a circuit from the anode to the cathode in the shortest and fastest way. Note that the current density is proportional to the reaction rate. This also accounts for the reason why reaction rate or reactant gases consumption was highest in the land area. For unsteady state, the average current density may vary with respect to time. Namely, the average current density at $t = 0.50$ s (Case 1) was 0.624 A cm^{-2} and at $t = 0.53$ s (Case 2) was 0.616 A cm^{-2}. Due to a small change of average current density, it was not easier to observe the differences on current density distributions for both cases.

3.3.5. Liquid water effects on temperature distributions

The lowest temperature could be observed at the flow inlet where the flows with ambient temperature come in, and the temperature increases along the positive flow direction. The heat generation was due to the electrochemical reaction and Ohmic heating. Therefore, the highest temperature concentrates in the catalyst layers in which the reactions take place and the current is generated. In addition, the temperature distribution through the solid materials (including flow plates/collectors and solid phase of porous media) is also affected by the heat conduction process. Depending on different solid materials, the thermal conductivity may change, resulting in different temperature distributions in different solid layers as shown in Fig. 19a. Note that the temperature distribution in the collectors seemed to be uniform due to a high thermal conductivity of the collector material. By controlling the convective coefficient h (Eq. (36)) to cool the cell, the average temperature was in the range of 334–340 K.

Fig. 19b and c shows temperature distributions on the middle-plane of the cathode channel ($Y = 0.0015$ m) and catalyst layers (0.002305 m) for Cases 1 and 2, respectively. It was observed that the temperature distribution in Case 1 was higher than that in Case 2. The presence of liquid water induced a decrease of temperature at the location occupied by the droplets. Initially, water droplets were suspended in the channel where the temperature was the lowest in the fuel cell due to the convection effect. The temperature of initial droplets was set to be equal to the value of ambient temperature (300 K). As the time progressed, these droplets moved forward as the airflow direction in the channel and a portion of liquid water was transported through the porous media. It is noticeable that the temperature in the porous media was highest due to chemical reactions taking place on the catalyst layer. The low temperature of liquid water transferred to and the heat generated from the cathode catalyst layer resulted in an uneven temperature distribution on the porous media.

3.4. Average current density with respect to time

The average current density of the cell is presented with respect to time as shown in Fig. 20a and b. For the time period from 0 s to 0.5 s, the fuel cell operated without an addition of liquid water as shown in Fig. 20a. As the time progressed, the average current density slightly increased after the fuel cell operation was started. In this stage, liquid water was not taken into account and hence it did not influence the increase of average current density. Since a stable flow and species parameters was obtained, it could be observed that the average current density reached a constant value at 6246 A m^{-2} at $t = 0.4$ s. Fig. 20b shows that when the water droplets were added into the channel at $t = 0.5$ s, the average current density of the cell was no longer constant at a value of 6246 A m^{-2}. In contrast, the average current density tended to decrease. It could be realized that the presence of liquid water in the fuel cell is a main reason to decrease the current density of the cell. As mentioned, water in the form of liquid may hinder the gas transport, resulting in a concentration loss and therefore cause a reduction of the current density. However, this decrease was only maintained until the time $t = 0.508$ s at which the liquid water was mostly moved out of the channel except for some kept in the porous media. The absence of liquid water led to a gradual increase in the current density as the time progressed, as shown in Fig. 20b.

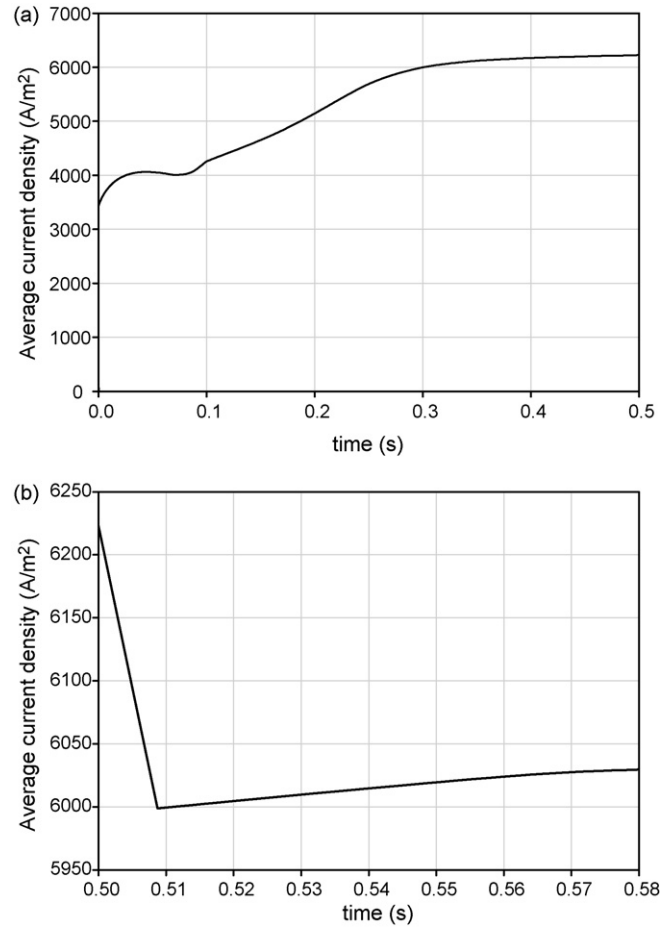

Fig. 20. The average current density of the cell vs. time (Case 2): (a) from $t = 0$ s to 0.50 s and (b) from $t = 0.50$ s to 0.58 s.

4. Conclusion

In this study, a three-dimensional, unsteady, multi-phase, multi-component PEMFC model with VOF interface tracking technique was solved using FLUENT® by developing own UDFs to customize the governing and relative equations. Numerical simulations were conducted for a single PEFMC with serpentine flow channels. This model considered all the necessary components consisting of a unit

PEMFC and coupled the fluid flow (momentum transport), species transport, energy transport, electron and proton transport, with volumetric electrochemical reactions. The membrane, gas diffusion layer and catalyst layers were treated as volumetric domain with grid points, and the electrochemical reactions in the catalyst layers as volumetric reactions. Especially, by using VOF interface tracking algorithm, the flow behaviors of liquid water and temperature field were also investigated. The main interpretations and conclusion of this study are summarized as follows:

1. The motion and behaviors of liquid water in a full 3D, unsteady PEMFC was completely described by using VOF interface tracking algorithm combined with solving the fluid flow, species transport, energy transport and electrochemical governing equations.
2. The motion of droplets in the PEMFC model was illustrated at different time steps in numerical simulation. Firstly, the droplets freely moved in the channel then deformed (elongation) in the flow direction, which was due to a combination of droplet surface tension and shear stress from surrounding airflow. After hitting the turning surface, these deformed droplets had the tendency of fragmenting and then entering the central airflow due to the dragging effect from the turning flow. Since the coalescence of water droplets was formed in the turning area resulting in a high concentration of liquid water volume, a substantial blockage in the channel occurred. After leaving the turning area, a significant shear stress from the airflow in the straight channel broke the coalescent droplets into smaller, discrete liquid droplets rather than deforming or elongating such water bands. Finally, liquid droplets were gradually removed out of the channel under a strong flow field.
3. The presence of liquid water in the channel significantly influences the flow field parameter. Namely, due to the blockage of water droplets, the gas flow would become unevenly distributed, the high pressure-drop regions would occur around the location of liquid droplets.
4. The structure of the channel will significantly influence the distribution of liquid water inside the cell. As simulated in a serpentine channel, the liquid water is difficult to be removed in the turning area. Therefore, a portion of liquid water tends to move through the gas diffusion layer in the porous media. By simulating different types of the channels, the characteristics of liquid water removal for different designs could be investigated.
5. By quantitatively and qualitatively analyzing the behaviors of liquid water and the average current densities at different periods of time, it could be observed that the liquid water would hinder the gas transport in the fuel cell, resulting in a high concentration loss and directly decreasing the current density—in other words, severely affect the fuel cell performance.
6. The local current density contours are also presented, showing that the high magnitude of the vectors mostly distribute in the region underneath the channel where high reaction rates exist.
7. By solving the energy equation, the temperature distribution over the fuel cell was described. The temperature was controlled at around 333 K by using a suitable forced convective coefficient applied on the fuel cell. The model also showed that the temperature of the channel and porous media with the presence of liquid water was lower than that without liquid water.

Acknowledgments

The authors are grateful for the support of this work by the Auto21™ Networks of Centers of Excellence (Grant D07-DFC), the Natural Sciences and Engineering Research Council of Canada (NSERC), the Canada Foundation for Innovation (CFI), the Ontario Innovation Trust (OIT), and the University of Windsor.

References

[1] S. Um, C.Y. Wang, K.S. Chen, J. Electrochem. Soc. 147 (2000) 4485.
[2] S. Dutta, S. Shimpalee, J.W. Van Zee, J. Appl. Electrochem. 30 (2000) 135.
[3] E. Hontanon, M.J. Escudero, C. Bautista, P.L. Garcia-Ybarra, L. Daza, J. Power Sources 86 (2000) 363.
[4] S.W. Cha, R. O'Hayre, Y. Saito, F.B. Prinz, J. Power Sources 134 (2004) 57.
[5] A.A. Kulikovsky, Electrochem. Commun. 3 (2001) 460.
[6] J.S. Yi, J.D. Yang, C. King, AIChE J. 50 (2004) 2594.
[7] H. Ju, G. Luo, C.Y. Wang, J. Electrochem. Soc. 154 (2007) B218.
[8] L. You, H. Liu, Int. J. Heat Mass Transfer 45 (2002) 2277.
[9] D. Natarajan, T.V. Nguyen, J. Power Sources 115 (2003) 66.
[10] T. Berning, N. Djilali, J. Electrochem. Soc. 150 (2003) A1589.
[11] S. Mazumder, J.V. Cole, J. Electrochem. Soc. 150 (2003) A1510.
[12] M. Vynnycky, M. Vynnycky, Appl. Math. Comput. 189 (2007) 1560.
[13] U. Pasaogullari, C.Y. Wang, J. Electrochem. Soc. 152 (2005) A380.
[14] H. Meng, C.Y. Wang, J. Electrochem. Soc. 152 (2005) A1733.
[15] Y. Wang, C.Y. Wang, J. Electrochem. Soc. 153 (2006) A1193.
[16] H. Meng, C.Y. Wang, Chem. Eng. Sci. 59 (2004) 3331.
[17] H. Ju, C.Y. Wang, J. Electrochem. Soc. 151 (2004) A1954.
[18] H. Ju, C.Y. Wang, S. Cleghorn, U. Beuscher, J. Electrochem. Soc. 153 (2006) A249.
[19] Y. Wang, C.Y. Wang, J. Power Sources 153 (2006) 130.
[20] P. Quan, B. Zhou, A. Sobiesiak, Z. Liu, J. Power Sources 152 (2006) 131.
[21] K. Jiao, B. Zhou, P. Quan, J. Power Sources 154 (2006) 124.
[22] K. Jiao, B. Zhou, P. Quan, J. Power Sources 157 (2006) 226.
[23] X. Zhu, P.C. Sui, N. Djilali, J. Power Sources 172 (2007) 287.
[24] J.H. Nam, M. Kaviany, Int. J. Heat Mass Transfer 46 (2003) 4595.
[25] B. Markicevic, A. Bazylak, N. Djilali, J. Power Sources 171 (2) (2007) 706.
[26] J.I. Gostick, M.A. Ioannidis, M.W. Fowler, M.D. Pritzker, J. Power Sources 173 (1) (2007) 277.
[27] P.K. Sinha, C.Y. Wang, J. Electrochem. Acta 52 (28) (2007) 7936.
[28] H. Dohle, R. Jung, N. Kimiaie, J. Mergel, M. Muller, J. Power Sources 124 (2003) 371.
[29] U. Pasaogullari, C. Wang, Electrochem. Acta 49 (2004) 4359.
[30] S. Freni, G. Maggio, E. Passalacqua, Mater. Chem. Phys. 48 (1997) 199.
[31] K. Jiao, B. Zhou, J. Power Sources 169 (2007) 296.
[32] K. Jiao, B. Zhou, J. Power Sources 175 (2008) 106.
[33] Fluent® 6.2 Documentation, Fluent Inc., 2005.
[34] R.B. Bird, W.E. Steward, E.N. Lightfoot, Transport Phenomena, John Wiley & Sons, New York, 1960.
[35] F. Barbir, PEM Fuel Cells, Elsevier Academic Press, 2005.
[36] T. Springer, T. Zawodzinski, S. Gosttesfeld, J. Electrochem. Soc. 138 (1991) 2334.
[37] R. O'Hayre, S.-W. Cha, W. Colella, F.B. Prinz, Fuel Cell Fundamentals, John Wiley & Sons, New York, 2006.
[38] C.S. Peskin, J. Comput. Phys. 25 (1997) 220.
[39] J. Larminie, A. Dicks, Fuel Cell Systems Explained, 2nd ed., John Wiley & Sons, England, 2003.
[40] J.H. Ferziger, M. Peric, Computational Methods for Fluid Dynamics, 3rd ed., Springer, 2002.
[41] X.G. Yang, F.Y. Zhang, A. Lubawy, C.Y. Wang, Electrochem. Solid-State Lett. 7 (2004) A408.
[42] F.Y. Zhang, X.G. Yang, C.Y. Wang, J. Electrochem. Soc. 153 (2006) A225.
[43] X. Liu, H. Guo, C. Ma, J. Power Sources 156 (2006) 267.
[44] K.W. Feindel, L.P.-A. LaRocque, D. Starke, S.H. Bergens, R.E. Wasylishen, J. Am. Chem. Soc., Commun. 126 (37) (2004) 11436.
[45] I. Manke, Ch. Hartnig, M. Grünerbel, J. Kaczerowski, W. Lehnert, N. Kardjilov, A. Hilger, W. Treimer, M. Strobl, J. Banhart, Appl. Phys. Lett. 90 (2007) 184101.
[46] J.R. Davey, R. Mukundan, T. Rockward, J.S. Spendelow, D.S. Hussey, D.L. Jacobson, M. Arif, R.L. Borup, 212th ECS Meeting, Washington, October 2007.